Title

Dysfunction of cortical GABAergic neurons leads to sensory hyper-reactivity in a Shank3 mouse model of ASD.

Journal

Nature neuroscience, 23(4)

ISSN

1097-6256

Authors

Chen, Qian
Deister, Christopher A
Gao, Xian
et al.

Publication Date

2020-04-01

DOI

10.1038/s41593-020-0598-6

Peer reviewed

nature neuroscience

ARTICLES

https://doi.org/10.1038/s41593-020-0598-6

Check for updates

Dysfunction of cortical GABAergic neurons leads to sensory hyper-reactivity in a *Shank3* mouse model of ASD

Qian Chen[1,10], Christopher A. Deister[2,10], Xian Gao[1,3], Baolin Guo[3,4], Taylor Lynn-Jones[1], Naiyan Chen[1], Michael F. Wells[3], Runpeng Liu[1], Michael J. Goard[5,6], Jordane Dimidschstein[3,7], Shijing Feng[8], Yiwu Shi[9], Weiping Liao[9], Zhonghua Lu[8], Gord Fishell[3,7], Christopher I. Moore[2] ✉ and Guoping Feng[1,3] ✉

Hyper-reactivity to sensory input is a common and debilitating symptom in individuals with autism spectrum disorders (ASD), but the neural basis underlying sensory abnormality is not completely understood. Here we examined the neural representations of sensory perception in the neocortex of a *Shank3B*$^{-/-}$ mouse model of ASD. Male and female *Shank3B*$^{-/-}$ mice were more sensitive to relatively weak tactile stimulation in a vibrissa motion detection task. In vivo population calcium imaging in vibrissa primary somatosensory cortex (vS1) revealed increased spontaneous and stimulus-evoked firing in pyramidal neurons but reduced activity in interneurons. Preferential deletion of *Shank3* in vS1 inhibitory interneurons led to pyramidal neuron hyperactivity and increased stimulus sensitivity in the vibrissa motion detection task. These findings provide evidence that cortical GABAergic interneuron dysfunction plays a key role in sensory hyper-reactivity in a *Shank3* mouse model of ASD and identify a potential cellular target for exploring therapeutic interventions.

Autism spectrum disorders (ASD) are highly heritable neurodevelopmental disorders, characterized by abnormalities in social interaction, repetitive behaviors, language and deficits in communication[1,2]. Atypical sensory responses are now part of the ASD diagnostic criteria (DSM-5). These sensory abnormalities are broad but include hyper-reactivity/sensitivity to sensory input. Human functional MRI (fMRI)[3] and animal model studies[4,5] suggest that cortical circuit abnormalities could contribute to altered sensory representations, but a direct demonstration of this has been lacking. Among the cell types implicated, cortical GABAergic interneurons are gaining more attention. Interneuron dysfunction has been observed in many animal models of ASD[4–7]. Further, recent work has linked GABAergic neuronal defects to multisensory integration deficits in mouse models of ASD[4,8]. However, a direct causal link between cortical GABAergic interneuron dysfunction and sensory abnormalities in ASD has not been established.

In this study, we used *Shank3B* knockout (*Shank3B*$^{-/-}$) mice[9] as a model to explore the neural mechanisms underlying sensory abnormalities. SHANK3 (SH3 and multiple ankyrin repeat domains 3) is a critical postsynaptic scaffolding protein that is required for glutamatergic synaptic development and function[10]. Deletions and mutations of the *Shank3* gene cause Phelan-McDermid syndrome with high prevalence of ASD. Genetic deletions/mutations of the *Shank3* gene in mice leads to glutamatergic synaptic dysfunction and ASD-relevant behavioral abnormalities[9,11–14]. In this study, we trained *Shank3B*$^{-/-}$ mice and their WT littermates to perform a vibrissa motion detection task and found that *Shank3B*$^{-/-}$ mice were more sensitive to weak vibrissa deflections. To test whether the hypersensitivity has a neocortical basis, we used in vivo two-photon calcium imaging to monitor neuronal activity in the somatosensory cortex of both WT and *Shank3B*$^{-/-}$ mice. Calcium imaging revealed increased spontaneous and stimulus-evoked activity in pyramidal neurons, but reduced activity in interneurons in *Shank3B*$^{-/-}$ mice. Preferential deletion of *Shank3* from interneurons was also associated with pyramidal neuron hyperexcitability and sensory hypersensitivity. These data suggest that neocortical interneuron dysfunction in *Shank3B*$^{-/-}$mice is key to the emergence of abnormal pyramidal neuron hyperexcitability and sensory hypersensitivity in this monogenic model of ASD.

Stimulus hyper-reactivity in *Shank3B*$^{-/-}$ mice. To investigate whether *Shank3B*$^{-/-}$ mice exhibit any deficits in tactile sensitivity, we trained both *Shank3B*$^{-/-}$ mice and their WT littermates to perform a tactile detection task. Head-fixed and water-restricted mice were presented with randomly timed periodic vibrissae deflections (Fig. 1a) and could earn a water reward by licking within a 'report

[1]McGovern Institute for Brain Research, Department of Brain and Cognitive Sciences, Massachusetts Institute of Technology, Cambridge, MA, USA. [2]Department of Neuroscience, Brown University, Providence, RI, USA. [3]Stanley Center for Psychiatric Research, Broad Institute of MIT and Harvard, Cambridge, MA, USA. [4]Department of Neurobiology, School of Basic Medicine, Fourth Military Medical University, Xi'an, China. [5]Department of Molecular, Cellular, and Developmental Biology, University of California, Santa Barbara, Santa Barbara, CA, USA. [6]Department of Psychological & Brain Sciences, University of California, Santa Barbara, Santa Barbara, CA, USA. [7]NYU Neuroscience Institute, New York University Langone Medical Center, New York, NY, USA. [8]Guangdong Provincial Key Laboratory of Brain Connectome and Behavior, The Brain Cognition and Brain Disease Institute, Shenzhen Institutes of Advanced Technology, Chinese Academy of Sciences, Shenzhen, China. [9]Institute of Neuroscience and Department of Neurology of the Second Affiliated Hospital of Guangzhou Medical University, Key Laboratory of Neurogenetics and Channelopathies of Guangdong Province and the Ministry of Education of China, Guangzhou, China. [10]These authors contributed equally: Qian Chen, Christopher A. Deister. ✉e-mail: Christopher_moore@brown.edu; fengg@mit.edu

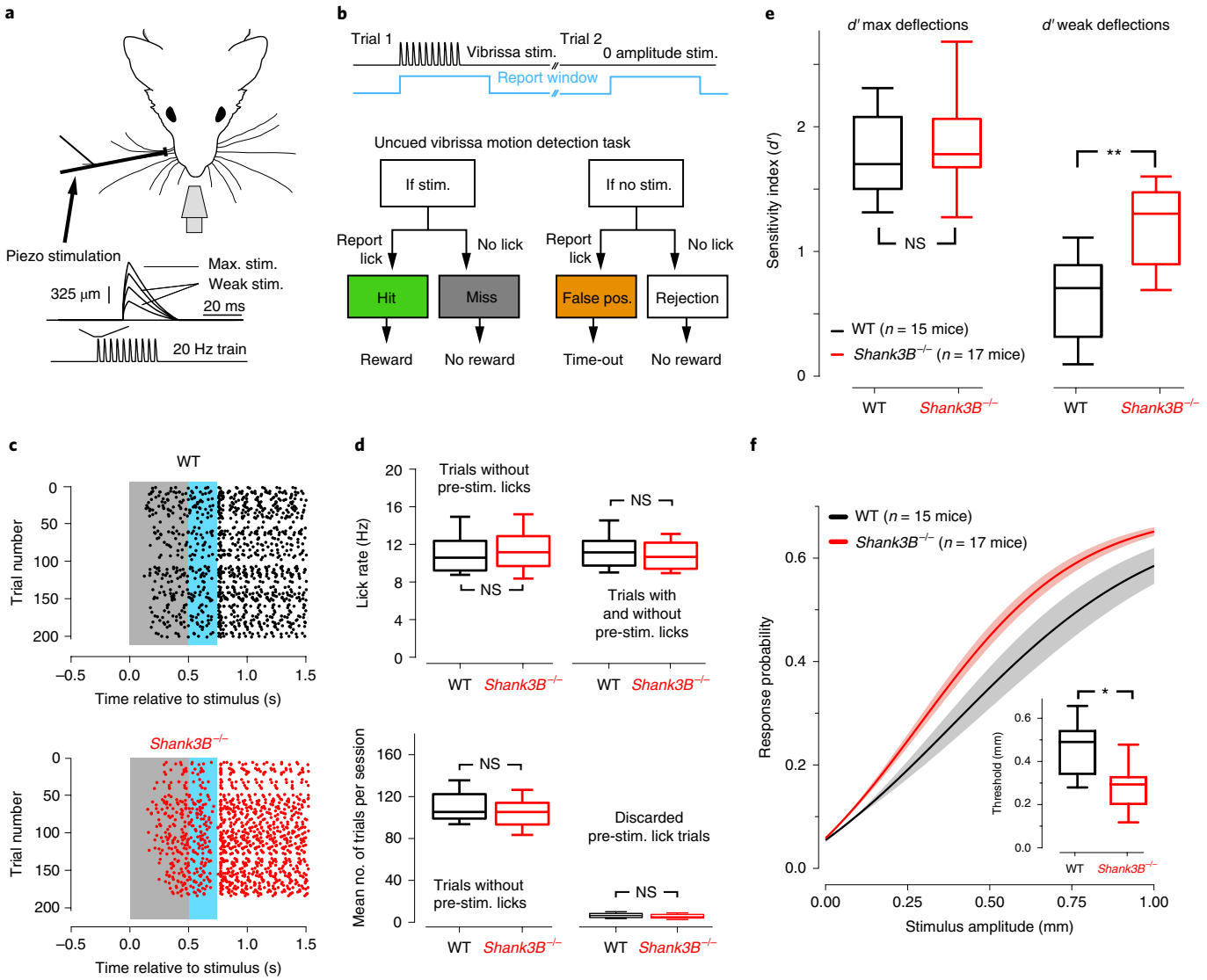

Fig. 1 | Vibrissa detection and stimulus hyper-reactivity in *Shank3B*$^{-/-}$ mice. a, Head-restrained mice were trained to lick at a waterspout when they detected vibrissa motion delivered via a piezo. The magnification shows the shape of an individual deflection, which had a variable amplitude between trials. **b**, Top: trials in the task consisted of a variable inter-trial interval (1–6.5 s), after which a stimulus was presented (black trace), which coincided with the triggering of a 'report window' (blue). Bottom: flow chart of the task. **c**, Example lick of a WT (top, black dots) and *Shank3B*$^{-/-}$ (bottom, red dots) in the late stage of training. Each dot represents a lick. These lick rasters show the distribution of individual licks as dots in a given trial relative to stimulus onset. The gray shaded region denotes the presence of stimuli and the blue shaded region denotes the report window. **d**, Top: box plots of mean lick rates for WT (black; $n=10$ mice) and *Shank3B*$^{-/-}$ (red; $n=10$ mice) animals. The left plots show the average lick rate for trials analyzed further in the study that showed no pre-stimulus licking. The right plots show the average lick rate including all trials discarded due to pre-stimulus licking. In either case, there was no significant difference in lick rates ($P=0.7$, $P=0.8$; bootstrap mean-difference test). Bottom: the left box plots show the average number of trials per session completed by WT (black) and *Shank3B*$^{-/-}$ (red) mice. The right box plots show the same as the left, but the average number of trials that were discarded per session because of pre-stimulus licking. There was no significant difference between WT and *Shank3B*$^{-/-}$ groups for either comparison ($P=0.8$, left; $P=0.6$, right; bootstrap mean-difference test). **e**, Box plots showing the sample distributions of the detection sensitivity (d') for strong (left) and weak (right) stimuli. Left: there was no statistical difference in the d' for strong (1 mm) whisker deflections (WT mean ± s.e.m.: 1.79 ± 0.10; black; *Shank3B*$^{-/-}$ mean ± s.e.m.: 1.8 ± 0.11, red; $n=15$ WT, $n=17$ *Shank3B*$^{-/-}$; $P=0.53$; bootstrap mean-difference test). Right: *Shank3B*$^{-/-}$ mice have a significantly higher d' for weak stimuli (WT mean ± s.e.m.: 0.59 ± 0.10; *Shank3B*$^{-/-}$ mean ± s.e.m.: 1.2 ± 0.09; $n=15$ WT, black; $n=17$ *Shank3B*$^{-/-}$ mice, red; $^{**}P<0.0001$; bootstrap mean-difference test). **f**, Mean psychometric curves (sigmoidal function fits) from the sessions used in **e**. Solid lines denote the mean, and the shaded regions are the s.e.m. The inset shows a significant difference of detection threshold between groups (WT mean ± s.e.m.: 449 ± 42 µm; *Shank3B*$^{-/-}$ mean ± s.e.m.: 296 ± 43 µm; n = 15 WT mice and 17 *Shank3B*$^{-/-}$ mice; $^{*}P=0.003$; bootstrap mean-difference test). There was also a difference in the unitless slope factor (WT mean ± s.e.m.: 232 ± 17; *Shank3B*$^{-/-}$ mean ± s.e.m.: 149 ± 18, $n=15$ WT mice and 17 *Shank3B*$^{-/-}$ mice; $P<0.0001$, bootstrap mean-difference test), which is a fit parameter related to the steepness of the curve. Box and whisker plots show median values (middle vertical bar) and 25th (bottom line of box) and 75th percentiles (top line of box) with whiskers indicating the range. All bootstrap mean-difference tests were two-sided. These results were repeated three times. Stim., stimulus.

window' that was timed to the onset of a stimulus (Fig. 1b, top). The frequency of the stimulus was fixed, but the strength was varied by scaling the amplitude (Fig. 1a, inset). The task was on a 'go/no-go' format and thus had four possible trial outcomes: a 'hit' if the animal licked correctly in response to a stimulus, a 'miss' if the animal did not lick when a stimulus was presented, a 'false positive'

if the animal licked in response to a zero-amplitude stimulus (catch trial), or a 'correct rejection' if the animal correctly ignored a zero-amplitude stimulus (Fig. 1b, bottom). The ratio of hits to all stimulus trials, and the ratio of false positives to all catch trials, were used to determine the hit rate and false positive rates (or false alarm rates). Using these estimates of hit and false-positive rates, the sensitivity index d-prime (d') was determined for each animal—which is a standard metric for scoring detection sensitivity from signal detection theory[15–17]. It is a metric that quantifies how separated an animal's responses to noise are from their responses to a true signal (Supplementary Fig. 1a). In addition to calculating d', we determined the related metric 'criterion location' to quantify an animal's bias towards reporting true positives versus false positives (Supplementary Fig. 1b). Criterion location is an important metric because animals can, in theory, improve their performance without a true change in sensitivity if they report more false positives (that is, by guessing more often). We found no differences in the relationship between d' and criterion between WT and *Shank3B*$^{-/-}$ animals (Supplementary Fig. 1c). Throughout the experiments, all littermate pairs of WTs and *Shank3B*$^{-/-}$ animals showed no differences in weight (mean weights ± s.e.m. of WT/*Shank3B*$^{-/-}$: first three sessions, 22.0 ± 3.0/23.6 ± 3.7 g; last three sessions, 21.6 ± 2.9/23.0 ± 3.9 g; $P = 0.68$ and $P = 0.54$, $n = 10$ in each group; bootstrap mean-difference test). Moreover, WT and *Shank3B*$^{-/-}$ mice did not show differences in their lick rates (Fig. 1d), which we assessed to rule out the potential of motor differences between WT and *Shank3B*$^{-/-}$ mice. Figure 1c shows lick rasters from a WT (Fig. 1c, top) and a littermate *Shank3B*$^{-/-}$ mouse (Fig. 1c, bottom). The data shown in Fig. 1c, which included all trials that showed no pre-stimulus licking, were compared across sessions and animals and showed no rate differences between WT and *Shank3B*$^{-/-}$ groups (Fig. 1d, top graph, left). We also found no difference in lick rates between WT and *Shank3B*$^{-/-}$ mice, even if trials with pre-stimulus licking were included (Fig. 1d, top graph, right). There was no significant difference in the total number of trials performed per session (Fig. 1d, bottom graph, left). Moreover, there was no difference in the number of trials discarded due to pre-stimulus licking (Fig. 1d, bottom graph, right), suggesting that both groups of mice had similar levels of impulsivity.

To compute d' and construct psychometric detection curves, we first computed the hit rate and false alarm rate for all stimuli across six sessions in which the animals' experience with the task overlapped (Supplementary Fig. 2a). Previous work has shown that somatosensory cortex contributes most to the detection of weak stimuli, closer to perceptual threshold[16,18]. Thus, we examined detection performance with respect to strong, readily detectable maximal stimuli (1 mm), and more ambiguous weak stimuli (0.2–0.5 mm) (Supplementary Fig. 2). False alarm rates appeared similar for WT and *Shank3B*$^{-/-}$ mice. We further analyzed the trials that comprised the last three overlapping sessions where performance had stabilized for all mice (Supplementary Fig. 2). First, we examined sensitivity differences by computing d' for strong and weak stimuli. Maximal d' for *Shank3B*$^{-/-}$ and WT animals was not significantly different (Fig. 1e, left). However, d' for weaker stimuli computed for the same behavioral sessions was significantly higher in *Shank3B*$^{-/-}$ when compared to WT animals (Fig. 1e, right). We then constructed psychometric curves for *Shank3B*$^{-/-}$ and WT mice (Fig. 1f) by determining hit rates for a range of stimulus amplitudes. The psychometric curve of *Shank3B*$^{-/-}$ mice show a leftward shift relative to WT mice. We quantified this shift by comparing the thresholds in our samples. We found that the threshold for WT mice was significantly higher than that of *Shank3B*$^{-/-}$ mice (Fig. 1f insets). Taken together, these data show that *Shank3B*$^{-/-}$mice are more sensitive than their WT counterparts to vibrissae stimuli.

Increased spontaneous and stimulus-evoked neuronal activity in *Shank3B*$^{-/-}$ mice. To study network mechanisms underlying stimulus hypersensitivity in *Shank3B*$^{-/-}$ mice, we performed large-scale in vivo two-photon calcium imaging in head-fixed awake WT and *Shank3B*$^{-/-}$ mice. We used the excitatory-specific human CaMKIIα promotor to drive the expression of the genetically encoded calcium indicator GCaMP6f (referred throughout as GCaMP6)[19]. Our imaging fields contained 68–112 neurons (mean ± s.e.m. 84 ± 12). First, we compared the spontaneous GCaMP6 activity of vS1 between *Shank3B*$^{-/-}$and WT mice. Interestingly, we found that *Shank3B*$^{-/-}$ mice showed higher calcium event rates compared to their WT counterparts (Fig. 2a,b). Between our sample groups, we observed a small but significant increase in pairwise correlation of spontaneous firing in *Shank3B*$^{-/-}$ mice (Fig. 2a, example traces; Fig. 2c). It is well established that when neuronal rate increases correlations will also increase, even beyond increases in chance spike overlap due to more spikes being discharged[18]. Although many factors could lead to different correlations between neurons, despite those neurons firing at the same rate under different conditions, one factor that has been previously studied is changing the balance of excitation and inhibition[20]. We studied the relationship between pairwise rate and

Fig. 2 | Enhanced spontaneous and stimulus-evoked activity in *Shank3B*$^{-/-}$ excitatory neurons. a, Top: example mean two-photon CaMKII-GCaMP6 imaging fields from a WT (left) and *Shank3B*$^{-/-}$ (right) mouse. Scale bar, 50 µm. Bottom: example spontaneous $\Delta F/F$ time series traces from the upper imaging fields from a WT (left) and *Shank3B*$^{-/-}$ (right) mouse. **b**, Box plots quantifying differences in spontaneous calcium event rates that were determined by counting the total number of deconvolved individual calcium events for 10 min ($n = 612$ neurons from 6 WT mice; 653 neurons from 6 *Shank3B*$^{-/-}$ mice). Asterisks denote a statistically significant difference between the sample groups (**$P < 0.0001$; bootstrap mean-difference test). **c**, The correlation between spontaneous firing was quantified as the Spearman's rank correlation coefficient (ρ). Box plots show the distribution of all pooled correlations between WT and *Shank3B*$^{-/-}$ excitatory neurons ($n = 65{,}931$ pairs from 6 WT mice; $n = 65{,}092$ pairs from 6 *Shank3B*$^{-/-}$ mice), and show an overall increase in correlations among excitatory neurons in *Shank3B*$^{-/-}$ compared to WT. Asterisk denotes a statistically significant difference between the sample groups (*$P = 0.004$; bootstrap mean-difference test). **d**, Example traces showing the $\Delta F/F$ responses to maximal (1 mm) whisker deflections stimulus of the responsive neurons from representative WT and *Shank3B*$^{-/-}$ mice. The dashed line indicates the onset of the whisker stimulus. **e**, Box plots showing the fraction of neurons determined to be stimulus responsive in WT ($n = 6$) and *Shank3B*$^{-/-}$ ($n = 6$) mice. The asterisk denotes a statistically significant difference between the sample groups (*$P = 0.002$; bootstrap mean-difference test). **f**, Left: the magnitude of evoked responses in WT mice, across the range of stimulus amplitudes. We quantified this by constructing peri-stimulus time histograms (PSTHs) from Z-scored evoked responses for all of the responsive neurons ($n = 107$ from 6 WT mice, $n = 93$ from 6 *Shank3B*$^{-/-}$ mice). The average response for each stimulus amplitude is color coded as indicated by the inset showing the piezo stimulus waveform (red is the maximal deflection and purple is the weakest). Lines on all plots indicate the mean and the shaded regions correspond to the s.e.m. Right: same as in the left panel, but from *Shank3B*$^{-/-}$ mice. **g**, Comparison of peak evoked responses across the stimulus amplitudes tested for responsive neurons ($n = 107$ from 6 WT mice and $n = 93$ from 6 *Shank3B*$^{-/-}$ mice. The centre of the circles represents the mean and the error bars represent the s.e.m. Asterisks denote statistically significant differences; $n = 107$ from 6 WT mice; $n = 93$ from 6 *Shank3B*$^{-/-}$ mice, *$P < 0.05$; NS, no difference ($P > 0.05$); bootstrap mean-difference test; P values in order from left to right: 0.24, 0.75, 0.03, 0.03, 0.04, 0.75. These results were repeated three times. Box and whisker plots show median values (middle vertical bar) and 25th (bottom line of the box) and 75th percentiles (top line of the box) with whiskers indicating the range. All bootstrap mean-difference tests were two-sided.

correlations by computing the geometric pairwise mean and correlation for all pairs in each imaging session. We then pooled these data and took the mean and standard error of the mean for three overlapping rate bins (Supplementary Fig. 3a). For WT mice there was a linear dependence on rate and correlation (linear fit; regression slope = 0.2; $P = 0.03$, linear regression F-test). For *Shank3B*$^{-/-}$, the correlation/rate relationship was relatively flat across the rates examined (linear fit; regression slope = 0.02, $P = 0.43$, linear regression F-test). These results suggest that the correlation increases in *Shank3B*$^{-/-}$ are the result of circuit alterations and not just a simple rate change.

We next determined if stimulus-evoked responses were also enhanced in *Shank3B*$^{-/-}$ mice. We performed in vivo two-photon imaging of excitatory neurons as mice received randomly timed and variable amplitude piezo-driven vibrissa deflections (Fig. 2f, inset), just as in our detection task. Figure 2d shows representative examples that are the evoked response from all stimulus-responsive neurons in a WT and *Shank3B*$^{-/-}$ imaging session. The average proportion of stimulus-responsive neurons found in WT mice was 0.26 ± 0.08 (mean ± s.e.m.), which is within the range of previous studies in vS1 of awake mice[21–23]. However, the proportion of stimulus-responsive neurons in *Shank3B*$^{-/-}$ mice was significantly higher

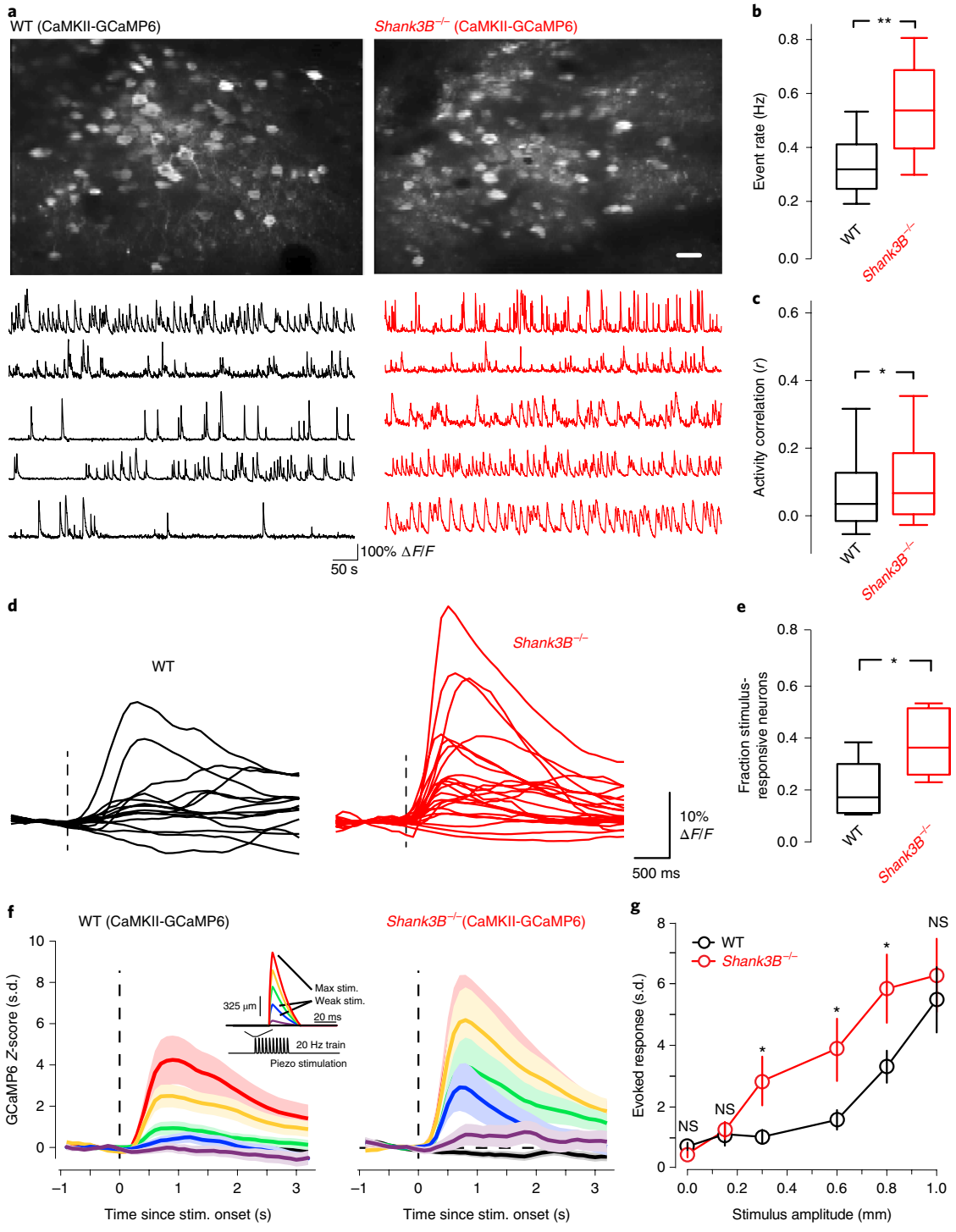

at 0.52 ± 0.11 (Fig. 2e, mean ± s.e.m.). In addition to an increase in the proportion of stimulus-responsive neurons in *Shank3B*$^{-/-}$ mice compared to WT, we found enhanced evoked responses across most of the range of stimulus amplitudes used in our detection task. To quantify this, we constructed average peri-stimulus time histograms (PSTHs, see Methods) for WT and *Shank3B*$^{-/-}$ mice (Fig. 2f). Visual comparisons of the WT and *Shank3B*$^{-/-}$ PSTHs showed clear differences, with an overall enhancement of *Shank3B*$^{-/-}$ activity. To more quantitatively compare these differences, we plotted the mean peak evoked response (Fig. 2g) for both WT and *Shank3B*$^{-/-}$. The strongest and weakest deflections showed no significant difference (Fig. 2g). As in our behavior, we found the largest differences in evoked responses around the intermediate stimulus range. These results show that layers II/III pyramidal neurons in vS1 of *Shank3B*$^{-/-}$ are more active and sensitive to external stimuli.

***Shank3B*$^{-/-}$ mice showed hypo-neuronal activity in inhibitory somatosensory cortical neurons.** *Shank3* is a major scaffolding protein at glutamatergic synapses, coordinating the recruitment of many postsynaptic signaling molecules[10,24]. It has been shown that *Shank3* deletion causes a reduction in glutamatergic synaptic transmission[9,11,14,25]. Interestingly, our calcium imaging results showed increased activity of cortical pyramidal neurons in *Shank3B*$^{-/-}$ animals. Sparse stimulus-evoked activity in layers II/III of WT vS1 is known to be dependent on stimulus-evoked feedforward inhibition[22,26,27], which is a mechanism that 'balances' stimulus-evoked feedforward excitation using strong, time-lagged inhibition[26–28]. Recently, deficits in parvalbumin circuits within the insular cortex and vS1 of *Shank3B*$^{-/-}$ mice have been reported[4,29]. We hypothesized that inhibitory circuit disruption in somatosensory cortex may cause excitatory neuron hyperactivity in *Shank3B*$^{-/-}$ mice. To test this, we performed two-photon calcium imaging selectively from inhibitory neurons of the vS1. We performed unilateral injections of adeno-associated viruses (AAVs) expressing GCaMP6 under the control of the GABAergic interneuron-specific Dlx5/6 promoter, a recently developed tool for GABAergic interneuron-specific expression[30]. We injected AAV-Dlx5/6-GCaMP6 into vS1, which resulted in selective expression of GCaMP6 in inhibitory neurons of vS1. As predicted, *Shank3B*$^{-/-}$ mice showed reduced spontaneous calcium event rates (Fig. 3a,b). Correlations in the spontaneous firing of inhibitory neurons in WT and *Shank3B*$^{-/-}$mice were more pronounced than excitatory neurons (Fig. 3a, example traces; Fig. 3c). Because we observed a significant decrease in firing rate of inhibitory neurons, an increase in correlations is not likely to be the result of a simple change in the rate of the population. We studied the relationship between rate and correlation, and found this relationship was not simply linear in either WT or *Shank3B*$^{-/-}$mice (Supplementary Fig. 3b). It shows high correlations between low-rate pairs and high-rate pairs, whereas moderate-rate pairs have low correlations. Overall, there was an increase in mean correlation among low- and high-rate pairs in *Shank3B*$^{-/-}$ mice.

We also examined stimulus-evoked activity in inhibitory cells, as we had for excitatory cells (Fig. 3d). We found the number of stimulus-responsive neurons was significantly reduced in *Shank3B*$^{-/-}$mice (Fig. 3e). Further, a comparison of PSTHs constructed from all stimulus-responsive inhibitory cells in WT and *Shank3B*$^{-/-}$ neurons revealed that over most of the stimulus range *Shank3B*$^{-/-}$ inhibitory cells showed significantly lower-magnitude responses than WT mice (Fig. 3f, g). Thus, inhibitory neurons in vS1 of *Shank3B*$^{-/-}$ are hypoactive.

Preferential *Shank3* deletion in vS1 interneurons causes interneuron hypo-excitability and excitatory neuron hyperexcitability. It remains unclear whether *Shank3* deletion in interneurons is the cause of the hyperactivity of the pyramidal neurons, or the downregulation of interneuron activity is an indirect byproduct of a lifetime of abnormal circuit development in these mice. To address this, we aimed to delete *Shank3* in the inhibitory neurons of vS1 using the Dlx5/6 promotor-driven Cre recombinase in the *Shank3B* conditional mice (*Shank3B*$^{fl/fl}$) that we generated[29]. Previously, the Dlx5/6 promotor was characterized to be highly selective in expressing fluorescent and optogenetic-proteins in inhibitory neurons, but its ability to restrict Cre expression to inhibitory cells was not found to be consistent in all cases, because trace amount of Cre could be sufficient for recombination[30]. To determine how selective an AAV-Dlx5/6-Cre-mKate2 (Dlx5/6-Cre) construct is at deleting *Shank3* in interneurons, we performed single-cell PCR from neighboring inhibitory and excitatory layer II/III vS1 neurons (Supplementary Fig. 4). We screened 42 excitatory neurons and 33 inhibitory neurons from three AAV-Dlx5/6-Cre-injected *Shank3B*$^{fl/fl}$ mice. *Shank3* was deleted in every inhibitory neuron examined. However, 23.15 ± 3.34% of the excitatory neurons also showed *Shank3* deletion. Thus, the use of the Dlx5/6-Cre construct in vS1 of *Shank3B*$^{fl/fl}$ mice leads to preferential deletion of *Shank3* in inhibitory interneurons.

Fig. 3 | Reduced spontaneous and stimulus-evoked activity in *Shank3B*$^{-/-}$ inhibitory neurons. a, Top: example mean two-photon Dlx5/6-GCaMP6 imaging fields from a WT (left) and *Shank3B*$^{-/-}$ (right) mouse. Scale bar, 50 µm. Bottom: example spontaneous $\Delta F/F$ time series traces from the upper imaging fields from a WT (left) and *Shank3B*$^{-/-}$ (right) mouse. **b**, Box plots quantifying differences in spontaneous calcium event rates that were determined by counting the total number of deconvolved individual calcium events for 10 min ($n = 382$ neurons from 6 WT mice; 402 neurons from 6 *Shank3B*$^{-/-}$ mice). Asterisks denote a statistically significant difference between the sample groups (**$P < 0.0001$; bootstrap mean-difference test). **c**, The correlation between spontaneous firing was quantified as the Spearman's rank correlation coefficient (ρ) for all possible pairings in each imaging session, and then pooled across sessions. Box plots show the distribution of all pooled correlations between WT and *Shank3B*$^{-/-}$ inhibitory neurons ($n = 39{,}018$ pairs from 6 WT mice; 43,954 pairs from 6 *Shank3B*$^{-/-}$ mice) and show an overall increase in correlations among inhibitory neurons in *Shank3B*$^{-/-}$ compared to WT. Asterisks denote a statistically significant difference between the sample groups (**$P < 0.0001$, bootstrap mean-difference test). **d**, Example traces showing the $\Delta F/F$ responses to maximal (1 mm) whisker deflections stimulus of the responsive neurons from representative WT and *Shank3B*$^{-/-}$ mice. The dashed line indicates the onset of the whisker stimulus. **e**, Box plots showing the fraction of neurons determined to be stimulus responsive in WT ($n = 6$) and *Shank3B*$^{-/-}$ ($n = 6$) mice. The asterisk denotes a statistically significant difference between the sample groups (mean proportion WT = 0.58 ± 0.05, $n = 6$ mice; mean proportion *Shank3B*$^{-/-}$ = 0.28 ± 0.06, $n = 6$ mice; *$P = 0.0002$; bootstrap mean-difference test). **f**, Left: the magnitude of evoked responses in WT mice, across the range of stimulus amplitudes. We quantified this by constructing PSTHs from *Z*-scored evoked responses for all of the responsive neurons ($n = 237$ from 6 WT mice, $n = 114$ from 6 *Shank3B*$^{-/-}$ mice). The average response for each stimulus amplitude is color coded as indicated by the inset showing the piezo stimulus waveform (red is the maximal deflection and purple is the weakest). Lines indicate the mean and the shaded regions correspond to the s.e.m. Right: same as in the left panel, but from *Shank3B*$^{-/-}$ mice. **g**, Comparison of peak evoked responses across the stimulus amplitudes tested for WT and *Shank3B*$^{-/-}$ mice ($n = 237$ from 6 WT mice, $n = 114$ from 6 *Shank3B*$^{-/-}$ mice). Centre of circles represent the mean and the error bars indicate s.e.m.; asterisks denote statistically significant differences (NS, no difference $P > 0.05$; *$P < 0.05$, **$P < 0.0001$, bootstrap mean-difference test; *P* values in order from left to right: 0.5, 0.6, 0.9, 0.001, <0.0001, <0.0001). These results were repeated three times. Box and whisker plots show median values (middle vertical bar) and 25th (bottom line of the box) and 75th percentiles (top line of the box) with whiskers indicating the range. All bootstrap mean-difference tests were two-sided.

For controls, we used a construct in which the catalytic domain of Cre recombinase was deleted (AAV-Dlx5/6-ΔCre-mKate2, Dlx5/6-ΔCre). We used AAV-Dlx5/6-GCaMP6 to monitor activity of inhibitory neurons in vS1. Strong GCaMP6 signal in layer II/III inhibitory neurons was detected by two-photon microscopy in both Dlx5/6-ΔCre and Dlx5/6-Cre virus-injected *Shank3B*$^{fl/fl}$ mice (Fig. 4a). Compared with Dlx5/6-ΔCre-injected *Shank3B*$^{fl/fl}$ mice, those neurons infected with Dlx5/6-Cre showed significantly lower calcium event frequency among inhibitory neurons, similar to that seen in *Shank3B*$^{-/-}$ mice (Fig. 4a,b). We observed an increase in spontaneous activity correlations among inhibitory cells (Fig. 4a, example traces; Fig. 4c), just as we did for inhibitory cells in the *Shank3B*$^{-/-}$ mouse. The relationship between rate and correlation for inhibitory neurons in the local knockout condition was very similar to that of the *Shank3B*$^{-/-}$ mouse, but overall the differences between Dlx5/6-ΔCre- and Dlx5/6-Cre-injected mice were more pronounced (Supplementary Fig. 3c). Also similar to *Shank3B*$^{-/-}$ mice, Dlx5/6-Cre-injected (local *Shank3B* knockout) mice showed more lower-rate pairs with higher correlations, and some high-rate pairs that also showed increases.

We also examined stimulus-evoked activity in inhibitory neurons in those mice. The proportion of stimulus responsive neurons was significantly reduced in Dlx5/6-Cre-injected *Shank3B*$^{fl/fl}$ mice (Fig. 4d,e). PSTHs show reduced evoked activity in Dlx5/6-Cre-injected mice relative to Dlx5/6-ΔCre-injected *Shank3B*$^{fl/fl}$ mice (Fig. 4f). These differences were significant for all of the stimulus amplitudes (Fig. 4g). These results show that preferential deletion of *Shank3* in GABAergic interneurons can cause hypoactivity of layer II/III interneurons of vS1.

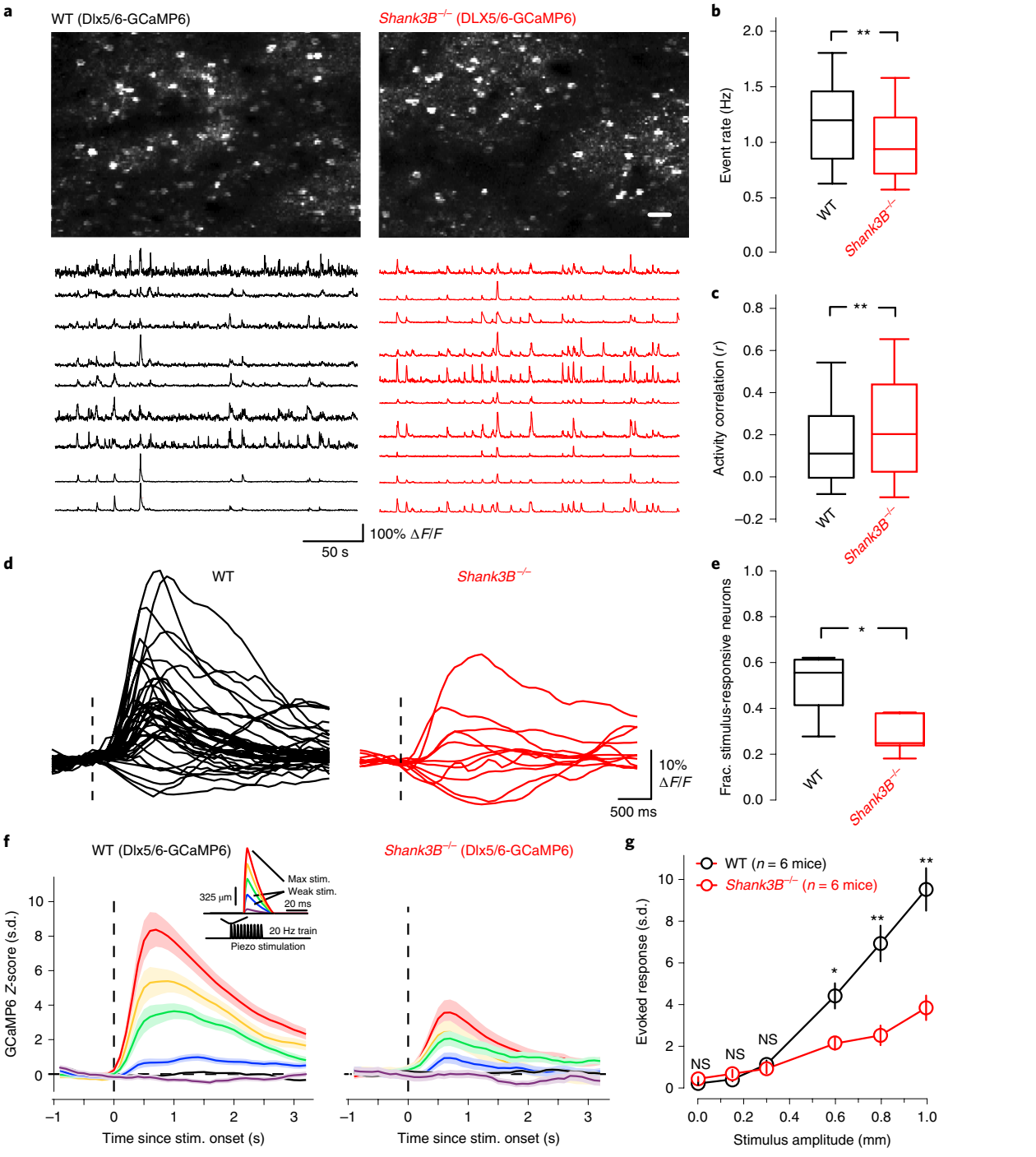

After establishing that *Shank3* deletion from inhibitory cells causes the hypo-excitability of interneurons, we hypothesized that the excitability of excitatory neurons would be consequently increased. To test this, we used the same strategy to delete *Shank3* from vS1 inhibitory neurons, but also monitored GCaMP6 activity in excitatory neurons by driving its expression via the CaMKII promoter (Fig. 5a). As predicted, the frequency of spontaneous calcium events was dramatically increased in Dlx5/6-Cre-injected *Shank3B*$^{fl/fl}$ mice (Fig. 5b,c and Supplementary Videos 1 and 2). In addition to an increase in excitatory neuron firing rates in the local knockout condition, we found that correlations in spontaneous firing was significantly increased in Dlx5/6-Cre-injected compared to Dlx5/6-ΔCre-injected *Shank3B*$^{fl/fl}$ mice. (Fig. 5b, example traces; Fig. 5d). For Dlx5/6-ΔCre-injected *Shank3B*$^{fl/fl}$ mice, there was a linear dependence on rate and correlation (Supplementary Fig. 3d; linear fit, regression slope = 0.21, $P = 0.03$, linear regression F-Test). For Dlx5/6-Cre-injected *Shank3B*$^{fl/fl}$ mice, the correlation/rate relationship was relatively flat across the rates examined (linear fit, regression slope = 0.02, $P = 0.6$, linear regression F-Test). These results are similar to those observed in WT/*Shank3B*$^{-/-}$ comparison, but the increase in correlations are higher in the local *Shank3B* knockout.

Evoked activity was also increased in excitatory neurons of Dlx5/6-Cre-injected mice. The proportion of excitatory neurons that were stimulus responsive was significantly higher in Dlx5/6-Cre-injected mice (Fig. 5e,f). Further, comparisons of PSTHs of stimulus-responsive neurons showed significant increases in the magnitude of vibrissa-evoked activity across all the stimulus amplitudes examined (Fig. 5g,h). Taken together, these results support the hypothesis that deletion of *Shank3* in interneurons results in a reduction of cortical inhibition, thereby increasing the amount of excitation in the cortical circuit.

Preferential deletion of *Shank3* in interneurons causes stimulus hyper-reactivity. It remains unclear if vS1-specific hyperexcitability will also lead to sensory hypersensitivity. To test this directly, we trained *Shank3B*$^{fl/fl}$ animals injected with AAV-Dlx5/6-Cre-mKate2 and injected with AAV-Dlx5/6-ΔCre-mKate2 for the detection task. The injected animals showed similar unilateral spread of Cre or ΔCre as measured by post-hoc examination of mKate2 expression in fixed tissue (Fig. 6a and Supplementary Fig. 5).

Similar to the results from WT and *Shank3B*$^{-/-}$ mice, we found that the relationship between apparent sensitivity (d') and response bias were the same between Dlx5/6-ΔCre- and Dlx5/6-Cre-injected mice (Supplementary Fig. 6). We also found no difference in weights between groups throughout the experiments (mean weights ± s.e.m. of Dlx5/6-Cre and Dlx5/6-ΔCre: first three sessions, 24.7 ± 2.6 g, 23.3 ± 3.2 g, $n = 6$ mice in each group, $P = 0.8$, bootstrap mean-difference test; last three sessions, 23.9 ± 2.4 g; 23.0 ± 3.1 g, $n = 6$ mice in each group, $P = 0.8$, bootstrap mean-difference test). Lick rates determined on just the analyzed trials that did not include those with pre-stimulus licks, or when we computed lick rate including discarded trials with pre-stimulus licks, were not significantly different between Dlx5/6-ΔCre- and Dlx5/6-Cre-injected mice (Fig. 6b, top). The average number of trials per session included for analysis were not different (Fig. 6b, bottom left), nor were the number of trials discarded per session (Fig. 6b, bottom right). To determine if Dlx5/6-Cre-injected mice were more sensitive than Dlx5/6-ΔCre, we computed d' for strong and weak stimuli. Maximal d' for Dlx5/6-ΔCre and Dlx5/6-Cre was significantly different (Fig. 6c, left). Further, d' for weaker stimuli computed for the same behavioral sessions was also significantly different between Dlx5/6-ΔCre and Dlx5/6-Cre animals (Fig. 6c, right). The psychometric curve of the Dlx5/6-Cre-injected mice was leftward shifted (Fig. 6d), indicating that their response rates to weaker stimuli are greater than Dlx5/6-ΔCre-injected mice. As predicted, Dlx5/6-Cre-injected mice had a lower threshold than Dlx5/6-ΔCre-injected mice (Fig. 6d inset).

Because we observed leakage of Dlx5/6-driven Cre expression in ~20% excitatory neurons, we set out to determine what effect sparse and selective deletion of *Shank3* from vS1 excitatory neurons, if any, would have on firing rates and detection behavior. We used diluted virus to titrate our injections and achieved ~40% infection of AAV-CaMKII-ΔCre-mKate2 (CaMKII-ΔCre) or AAV-CaMKII-Cre-mKate2 (CaMKII-Cre) excitatory neurons in vS1 of *Shank3B*$^{fl/fl}$ mice (Supplementary Fig. 7a,b). We found that the spontaneous activity and evoked response of excitatory neurons in CaMKII-Cre-injected *Shank3B*$^{fl/fl}$ mice were significantly reduced (Supplementary Fig. 7c–g). Overall detection performance was also

Fig. 4 | Reduced spontaneous and stimulus-evoked activity in inhibitory neurons after preferential deletion of *Shank3* in interneurons in vS1. a, Top: example mean two-photon Dlx5/6-GCaMP6 imaging fields from an AAV-Dlx5/6-ΔCre-mKate2-injected (left) and AAV-Dlx5/6-Cre-mKate2-injected (right) *Shank3B*$^{fl/fl}$ mouse. Scale bar, 50 μm. Bottom: example spontaneous $\Delta F/F$ time series traces from the top imaging fields from Dlx5/6-ΔCre-injected (left) and Dlx5/6-Cre-injected (right) *Shank3B*$^{fl/fl}$ mouse. **b**, Box plots quantifying differences in spontaneous calcium event rates that were determined by counting the total number of deconvolved individual calcium events for 10 min ($n = 432$ neurons from 6 Dlx5/6-ΔCre-injected mice; 407 neurons from 6 Dlx5/6-Cre-injected mice). Asterisks denote a statistically significant difference between the sample groups (**$P < 0.0001$; bootstrap mean-difference test). **c**, The correlation between spontaneous firing was quantified as the Spearman's rank correlation coefficient (ρ) for all possible pairings in each imaging session, and then pooled across sessions. Box plots show the distribution of all pooled correlations between Dlx5/6-ΔCre-injected (control group) and Dlx5/6-Cre-injected (local knockout group) inhibitory neurons ($n = 37{,}464$ pairs from 6 Dlx5/6-ΔCre-injected mice; $n = 35{,}372$ pairs from 6 Dlx5/6-Cre-injected mice), and show an overall increase in correlations among inhibitory neurons in Dlx5/6-Cre-injected compared to Dlx5/6-ΔCre-injected mice. Asterisks denote a statistically significant difference between the sample groups (**$P < 0.0001$; bootstrap mean-difference test). **d**, Example traces showing the $\Delta F/F$ responses to maximal (1 mm) whisker deflections stimulus of the responsive neurons from a representative Dlx5/6-ΔCre-injected (black) and Dlx5/6-Cre-injected (red) mice. The dashed line indicates the onset of the whisker stimulus. **e**, Box plots showing the fraction of neurons determined to be stimulus responsive neurons in Dlx5/6-ΔCre-injected ($n = 6$) and Dlx5/6-Cre-injected ($n = 6$) mice. Asterisk denotes a statistically significant difference between the sample groups (Dlx5/6-ΔCre group proportion = 0.39 ± 0.09, $n = 6$ mice; Dlx5/6-Cre group proportion = 0.16 ± 0.05, $n = 6$ mice; mean ± s.e.m.; *$P = 0.01$; bootstrap mean-difference test). **f**, Left: the magnitude of evoked responses in Dlx5/6-ΔCre-injected mice across the range of stimulus amplitudes was quantified by constructing PSTHs from Z-scored evoked responses for all of the responsive neurons ($n = 102$ from 6 Dlx5/6-ΔCre mice, $n = 58$ from 6 Dlx5/6-Cre mice). The average response for each stimulus amplitude is color coded as indicated by the inset showing the piezo stimulus waveform (red is the maximal deflection and purple is the weakest). Lines on all plots indicate the mean and the shaded regions correspond to the standard error of the mean. Right: same as in the left panel, but from Dlx5/6-Cre-injected mice. **g**, Comparison of peak evoked responses across the stimulus amplitudes tested for Dlx5/6-ΔCre-injected (black) and Dlx5/6-Cre-injected (red) mice ($n = 102$ from 6 Dlx5/6-ΔCre mice, $n = 58$ from 6 Dlx5/6-Cre mice). Asterisks denote statistically significant differences (*$P < 0.05$, **$P < 0.0001$; NS, no significant difference ($P > 0.05$); bootstrap mean-difference test, P values in order from left to right: 0.4, 0.003, <0.0001, <0.0001 and 0.03). Box and whisker plots show median values (middle vertical bar) and 25th (bottom line of the box) and 75th percentiles (top line of the box) with whiskers indicating the range. All bootstrap mean-difference tests were two-sided. ΔCre, AAV-Dlx5/6-ΔCre-mKate2-injected mouse group; Cre, AAV-Dlx5/6-Cre-mKate2-injected mouse group.

reduced in *Shank3B*$^{fl/fl}$ mice injected with CaMKII-Cre. The psychometric curve for CaMKII-Cre-injected *Shank3B*$^{fl/fl}$ mice ($n = 9$ mice) showed an in-significant increase in threshold relative to CaMKII-ΔCre-injected *Shank3B*$^{fl/fl}$ mice (Supplementary Fig. 7h). However, there was a reduction in performance of CaMKII-Cre-injected *Shank3B*$^{fl/fl}$ mice (Supplementary Fig. 7h). These data suggest that deletion of *Shank3B* just in a proportion of excitatory neurons does not improve stimulus sensitivity, as we observed in *Shank3B*$^{-/-}$ mice or the interneuron-biased local *Shank3B* knockout. Consistent with this, CaMKII-Cre and CaMKII-ΔCre-injected mice showed similar d' values for strong and weak stimuli (Supplementary Fig. 7i). The reason we observed a rightward shift in the psychometric curve without a reduction in d' was because false-alarm rates and stimulus-response rates were lowered by a similar proportion. Thus, *Shank3B* deletion in excitatory neurons leads to reduced spontaneous and evoked activity in excitatory neurons, as well as blunted detection behavior. Both of these results are qualitatively opposite of those observed in the *Shank3B*$^{-/-}$ mice, and the interneuron-biased local *Shank3B* deletion condition.

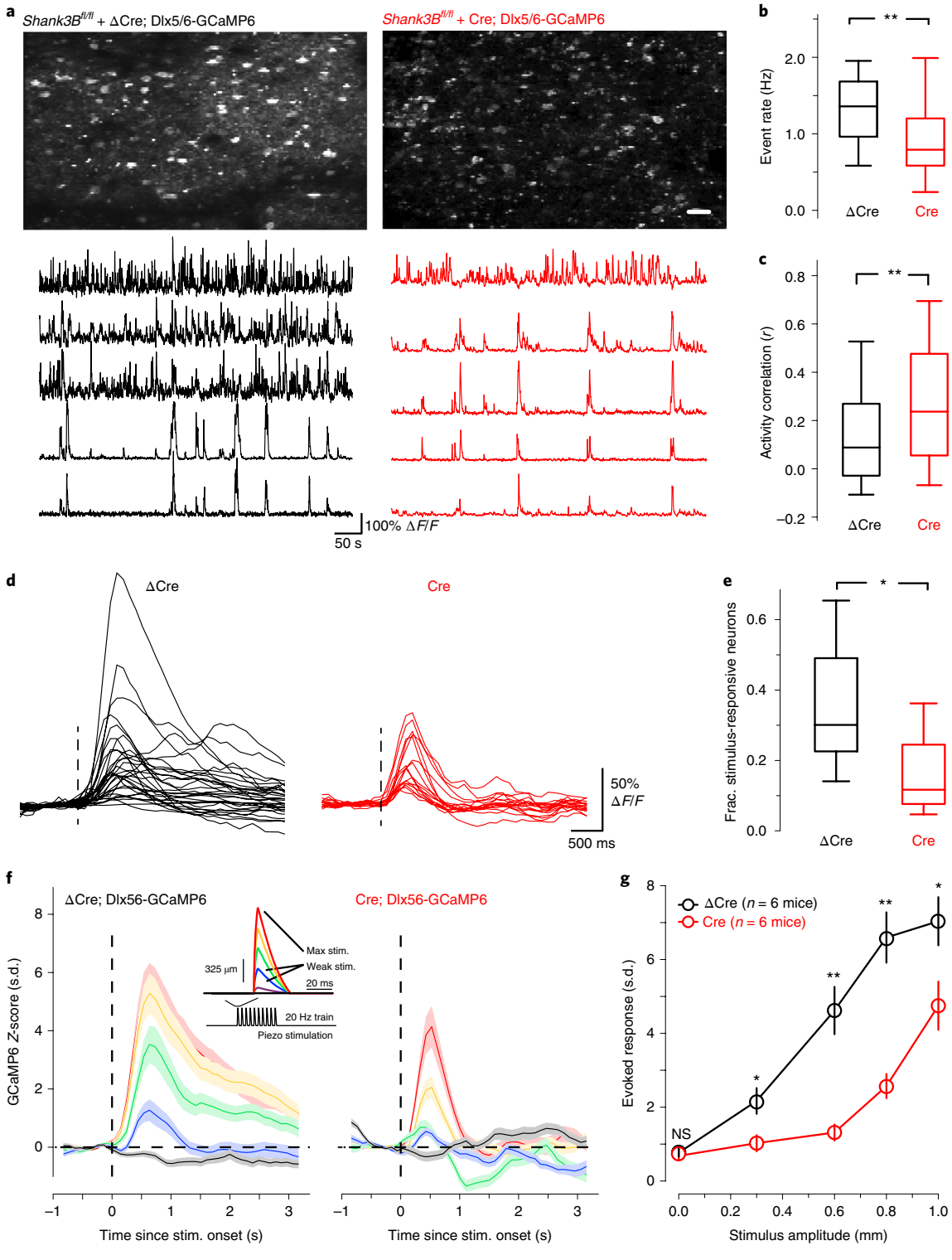

We next sought to determine if downregulation of inhibition alone was sufficient in explaining the results seen in network dynamics and detection performance observed in *Shank3B*$^{-/-}$ mice. Using an inhibitory chemogenetic approach, we injected an AAV-Dlx5/6-hM4Di in vS1 of WT mice. We made acute in vitro slices to determine the effectiveness of our Dlx5/6-hM4Di construct, and the DREADDs-agonist C21 (Supplementary Figs. 8a,b). We then imaged the activity of excitatory neurons using CaMKII-GCaMP6 in vivo from Dlx5/6-hM4Di-injected mice and trained them to perform the detection task. After mice showed proficiency in the task, we injected mice with the hM4Di agonist C21 (2 mg kg^{-1}) and imaged spontaneous and evoked neural activity as well as their performance on the detection task. We found an increase in spontaneous, evoked activity and correlation among excitatory neurons (Supplementary Figs. 8c–h), just as we had in the *Shank3B*$^{-/-}$condition, and the local Dlx5/6-driven *Shank3B* deletion. Chemogenetically driven inhibitory neuron downregulation led to markedly similar effects on detection-task performance as the local inhibitory neuron biased *Shank3B* knockout condition. We found that the *d′* for strong and weak whisker deflections were increased after injecting the DREADDs-agonist C21 (Fig. 6e). Psychometric curves showed a significant leftward shift after C21 injection (Fig. 6f). This result is consistent with precious findings in vS1 that optogenetically reducing the PV neuronal activity can enhance mouse performance in the detection task[31]. These results demonstrate that preferential deletion of *Shank3* from vS1 interneurons is sufficient to drive behavioral sensory hyper-reactivity.

Discussion

Sensory hypersensitivity has been observed in several mouse models of ASD and related neurodevelopmental disorders, including *Mecp2*$^{-/-}$ and *Fmr1*$^{-/-}$ [4,7] mice. Recent studies in ASD mouse models of *Mecp2*, *Shank3* and *Gabrb3* have shown that peripheral sensory neuron dysfunctions contribute to somatosensory defects including gentle touch[8,29]. Our results show that deficits in central nervous system circuits significantly contributes to sensory abnormalities in *Shank3B*$^{-/-}$ mice. The sensory hypersensitivity in *Shank3B*$^{-/-}$ mice correlates with a hyperactivity of cortical pyramidal neurons. Preferential deletion of *Shank3* in cortical inhibitory neurons is sufficient to cause a hyperactive cortical pyramidal neuron network and sensory hyper-reactivity. Impaired inhibitory neuron function has also been found in many other models of ASD[4,32,33]. Our current study provides evidence that dysfunctional excitatory synaptic transmission in cortical interneurons is likely to result in their hypoactivity and consequently contributes to sensory hyper-reactivity in the *Shank3* mouse model of ASD.

A significant proportion of autistic individuals experience perceptual abnormalities[2,34,35]. Although *Shank3* expresses throughout the brain, it is enriched at both cortico-striatal and cortico-cortical synapses[9,36,37] and could lead to deficits in both local and long-range cortico-cortical interactions. Recent work[4,38] indicated that the cortex of *Shank3B*$^{-/-}$ mice is in a hyperexcitable state throughout early development, ultimately contributing to abnormal associative interactions between cortex and striatum. To further understand the mechanisms responsible for the hyperexcitable state of *Shank3B*$^{-/-}$ mice, we focused on somatosensory cortex and used a head-fixed 'go/no-go'-based sensory detection task to probe perceptual disruptions in *Shank3B*$^{-/-}$ mice. These experiments showed an intrinsic stimulus sensitivity enhancement in *Shank3B*$^{-/-}$ mice. We found that motivational variables such as lick rates and criterion were similar across WT and *Shank3B*$^{-/-}$ animals and thereby allowed for fair comparisons of sensitivity measures across groups. The relatively short training time needed for WT animals to learn the detection task may prove to be an essential feature for probing perceptual abnormalities in disease models[15,17].

In addition to changes in rate among excitatory and inhibitory neurons, we observed increases in pairwise correlations between both types of cells in *Shank3B*$^{-/-}$ mice. For the excitatory neurons,

Fig. 5 | Preferential deletion of *Shank3* in vS1 interneurons also results in enhanced spontaneous and stimulus-evoked activity in excitatory neurons. **a**, Left: selective deletion of *Shank3* in the interneurons of somatosensory cortex was achieved by injection of interneuron-specific AAV-Cre virus (AAV-Dlx5/6-Cre-mKate2 or AAV-Dlx5/6-ΔCre-mKate2 as control) in *Shank3B*$^{fl/fl}$ mice. AAV-CaMKII-GCaMP6 (CaMKII-GCaMP6) virus was co-injected to monitor the neuronal activity in pyramidal neurons. Right: the confocal images of the GCaMP6 (green) and Dlx5/6-ΔCre/Cre expression (red) in an AAV-Dlx5/6-ΔCre-mKate2-injected (left) and AAV-Dlx5/6-Cre-mKate2-injected *Shank3B*$^{fl/fl}$ mouse (right). **b**, Top: example mean two-photon CaMKII-GCaMP6 imaging fields from a Dlx5/6-ΔCre (left) and Dlx5/6-Cre-injected (right) mouse. Scale bar, 50 μm. Bottom: example spontaneous Δ*F*/*F* time series traces from the top imaging fields from Dlx5/6-ΔCre-injected (left) and Dlx5/6-Cre-injected (right) mice. **c**, Box plots quantifying differences in spontaneous calcium event rates that were determined by counting the total number of deconvolved individual Ca^{2+} events for 10 min ($n = 486$ neurons from 6 Dlx5/6-ΔCre-injected mice; 510 neurons from 6 Dlx5/6-Cre-injected mice). Asterisks denote a statistically significant difference between the sample groups (**$P < 0.0001$; bootstrap mean-difference test). **d**, The correlation between spontaneous firing was quantified as the Spearman's rank correlation coefficient (ρ) for all possible pairings in each imaging session, and then pooled across sessions. Box plots show the distribution of all pooled correlations between Dlx5/6-ΔCre-injected (control group) and Dlx5/6-Cre-injected (local knockout group) excitatory neurons ($n = 38,874$ pairs from 6 Dlx5/6-ΔCre-injected mice; 40,178 pairs from 6 Dlx5/6-Cre-injected mice), and show an overall increase in correlations among excitatory neurons in Dlx5/6-Cre-injected compared to Dlx5/6-ΔCre-injected. Asterisks denote a statistically significant difference between the sample groups (**$P < 0.0001$; bootstrap mean-difference test). **e**, Example traces showing the Δ*F*/*F* responses to maximal (1 mm) whisker deflections stimulus of the responsive neurons from a representative Dlx5/6-ΔCre-injected and Dlx5/6-Cre-injected mice. The dashed line indicates the onset of the whisker stimulus. **f**, Box plots showing the fraction of neurons determined to be stimulus responsive in Dlx5/6-ΔCre-injected ($n = 6$) and Dlx5/6-Cre-injected ($n = 6$) mice. Asterisks denote a statistically significant difference between the sample groups (Dlx5/6-ΔCre proportion = 0.16 ± 0.06, $n = 6$ mice; Dlx5/6-Cre proportion = 0.35 ± 0.08, $n = 6$ mice; **$P < 0.0001$; bootstrap mean-difference test). **g**, Left: the magnitude of evoked responses in Dlx5/6-ΔCre-injected mice across the range of stimulus amplitudes. We quantified this by constructing PSTHs from *Z*-scored evoked responses for all of the responsive neurons ($n = 123$ neurons from 6 Dlx5/6-ΔCre-injected mice and 188 neurons from 6 Dlx5/6-Cre-injected mice). The average response for each stimulus amplitude is color coded as indicated by the inset showing the piezo stimulus waveform (red is the maximal deflection and purple is the weakest). Solid lines correspond to the mean and the colored shaded regions correspond to the standard error of the mean. Right: same as in the left panel, but from Dlx5/6-Cre-injected mice. **h**, Comparison of peak evoked responses across the stimulus amplitudes tested for all responsive neurons in Dlx5/6-ΔCre-injected ($n = 123$ neurons from 6 mice) and Dlx5/6-Cre-injected ($n = 188$ neurons from 6 mice) *Shank3B*$^{fl/fl}$ mice. The centre of the circles represents to the mean and the error bars represent to the standard error of the mean. Asterisks denote statistically significant differences (**$P < 0.0001$; NS, no difference $P > 0.05$; bootstrap mean-difference test, *P* values in order from left to right: 0.5, <0.0001, <0.0001, <0.0001, <0.0001, <0.0001). These results were repeated two times. Box and whisker plots show median values (middle vertical bar) and 25th (bottom line of the box) and 75th percentiles (top line of the box) with whiskers indicating the range. All bootstrap mean-difference tests were two-sided. ΔCre, AAV-Dlx5/6-ΔCre-mKate2-injected mouse group; Cre, AAV-Dlx5/6-Cre-mKate2-injected mouse group.

we found a net increase in both rate and correlations. It has been established in the theoretical literature that rate and correlation are inexorably linked, at least when neurons are driven to fire at different rates with excitation alone[18]. We found a significant relationship between rate and correlation among excitatory neurons in WT mice, but this relationship was altered to some degree in *Shank3B*$^{-/-}$ mice,

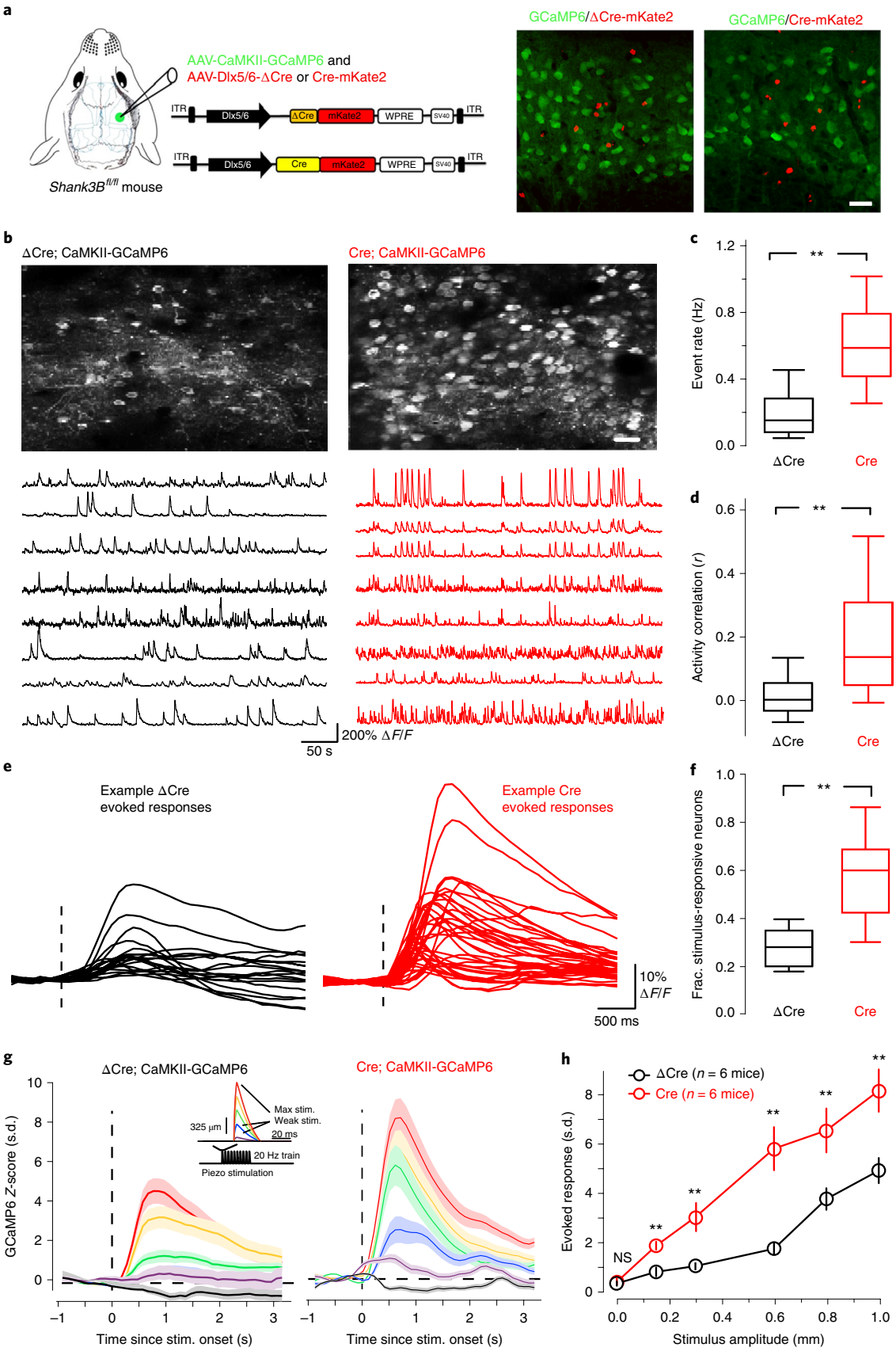

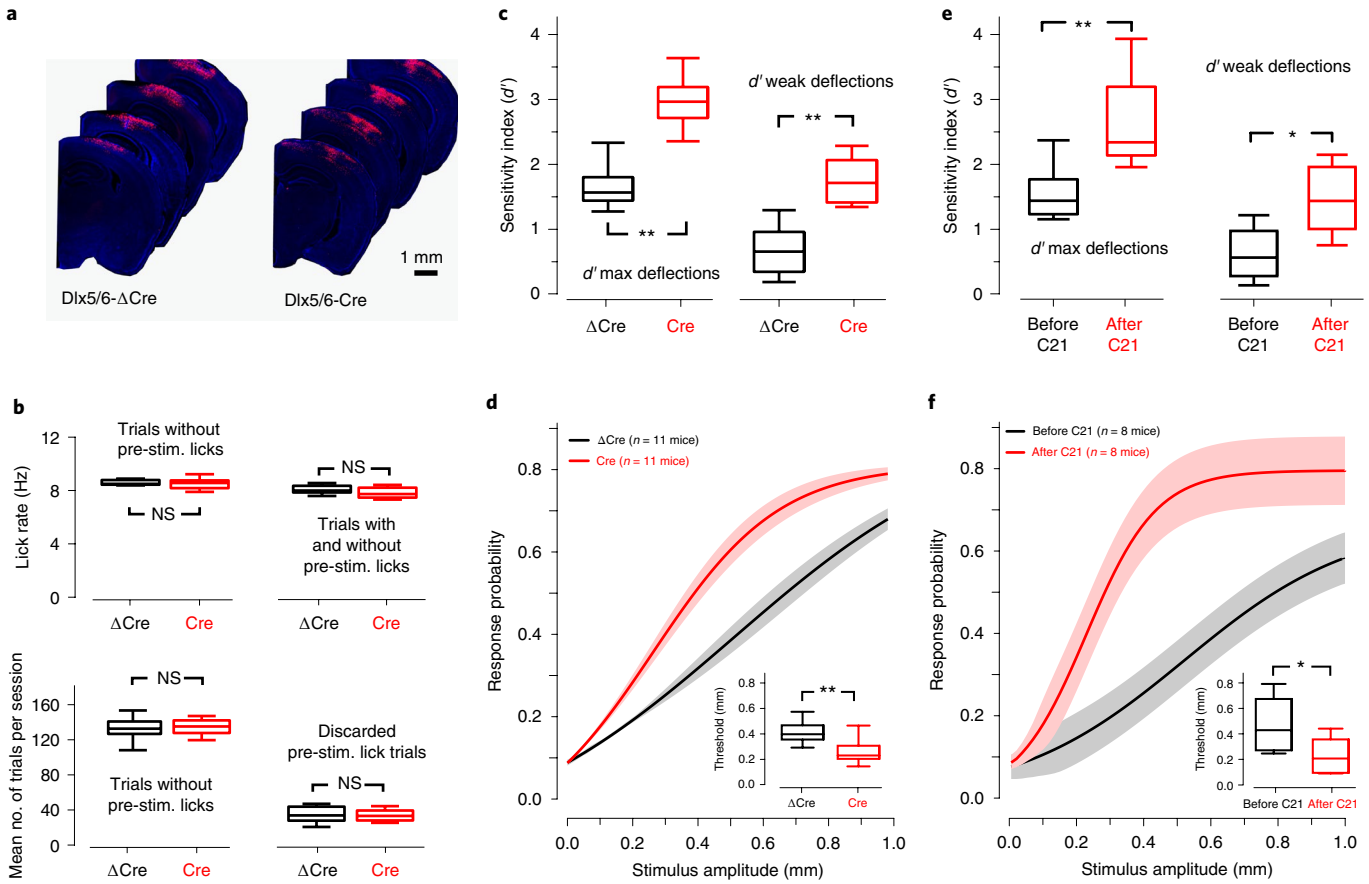

Fig. 6 | Preferential deletion of *Shank3* in interneurons of vS1 leads to behavioral hyper-reactivity of the somatosensory system. a, *Shank3B*$^{fl/fl}$ mice were injected with an AAV containing either a Dlx5/6-ΔCre or Dlx5/6-Cre construct in vS1. The image montage shows the extent of localization of ΔCre or Cre expression in two example mice. **b**, Top: box plots of mean lick rates for Dlx5/6-ΔCre (black) and Cre (red) injected animals. Left: average lick rate for trials that showed no pre-stimulus licking at all. Right: average lick rate including trials on the left and trials that showed pre-stimulus licking. In either case, there was no significant difference in lick rates (left, $P=0.8$; right, $P=0.5$; bootstrap mean-difference test). Bottom left: box plots showing the number of trials per session completed by Dlx5/6-ΔCre ($n=6$ mice) and Dlx5/6-Cre ($n=6$ mice) injected animals. ($P=0.7$; bootstrap mean-difference test). Right: same as left, but for the average number of trials with pre-stimulus licks (which were not analyzed). There was no significant difference ($P=0.8$; bootstrap mean-difference test). **c**, Left: box and whisker plots showing the bootstrap estimate of population mean d' for maximal stimuli for Dlx5/6-ΔCre ($n=11$ mice) and Dlx5/6-Cre ($n=11$ mice) injected animals. Right: same but showing d' for weak stimuli. There was a significant difference in both maximal d' (Dlx5/6-ΔCre mean ± s.e.m.: 1.59 ± 0.12; Dlx5/6-Cre: 2.92 ± 0.14, $^{**}P<0.0001$, bootstrap mean-difference test) and weak d' (Dlx5/6-ΔCre mean ± s.e.m.: 0.65 ± 0.13; Dlx5/6-Cre: 1.73 ± 0.12; $n=11$ mice for each group; $^{**}P<0.0001$, bootstrap mean-difference test). **d**, Mean psychometric curves (non-normalized sigmoidal function fits) from the same sessions used in **c**. Solid lines denote the mean, and the shaded regions are s.e.m. The inset show a significant difference of detection threshold between groups ($^{**}P<0.0001$; bootstrap mean-difference test, Dlx5/6-ΔCre mean ± s.e.m.: 416 ± 31 µm; Dlx5/6-Cre: 266 ± 35 µm; $n=11$ mice from each group). There was also a difference in the slope factors (Dlx5/6-ΔCre mean ± s.e.m.: 207 ± 13; Dlx5/6-Cre: 127 ± 17; n = 11 mice in each group $^{**}P<0.0001$, bootstrap mean-difference test). **e**, Left: box and whisker plots showing the bootstrap estimate of population mean d' maximal stimuli for the hM4Di-injected mice before and after C21 infusion ($^{**}P<0.0001$, bootstrap mean-difference test; before C21 mean ± s.e.m.: 1.58 ± 0.17; after C21 2.73 ± 0.31). Right: same but showing d' for weak stimuli (before C21 mean ± s.e.m.: 0.62 ± 0.16; after C21 1.46 ± 0.21; $n=8$ mice; $^{*}P=0.0002$, bootstrap mean-difference test). **f**, Mean psychometric curves (non-normalized sigmoidal function fits) from the same sessions used in **e**. Solid lines denote the mean, and the shaded regions are s.e.m. The inset show a significant difference of detection threshold between groups (pre-C21 mean ± s.e.m.: 525 ± 151 µm; post-C21 233 ± 55 µm; $n=8$ mice from each group; $^{*}P=0.004$; bootstrap mean-difference test). The slope factor was also significantly different (pre-C21 mean ± s.e.m.: 270 ± 65, post-C21: 114 ± 23; $n=8$ mice; $P=0.02$; bootstrap mean-difference test). These results repeated two times. Box and whisker plots show median values (middle vertical bar) and 25th (bottom line of the box) and 75th percentiles (top side of the box) with whiskers indicating the range. All bootstrap mean-difference tests were two-sided. ΔCre, AAV-Dlx5/6-ΔCre-mKate2-injected mouse group; Cre, AAV-Dlx5/6-Cre-mKate2-injected mouse group.

and the local Dlx5/6-Cre-driven *Shank3B* knockout mice. The specific cellular- and network-level reasons for this correlation change, and its importance, remain to be determined. However, excitatory and inhibitory conductance could influence neuronal correlations differently[20]. Therefore, it is possible that the increased correlations among excitatory neurons that we observed reflects a reduction in inhibition driven by *Shank3* deletion. We also observed a net increase in correlations among inhibitory neurons in the knockout conditions, and in those cases, the average rates were significantly decreased. Since inhibitory neurons are strongly coupled to each other, and inhibitory neuron activity is reduced when *Shank3* is deleted, we can hypothesize that the overall trend for correlations to increase among inhibitory cells is also due to a reduction of inhibitory conductance among them. Our data do not address why there

is a group of low firing rate inhibitory neurons with very high correlations in the WT mouse in the first place, or if they are truly distinct from the higher firing rate inhibitory neurons. What possible benefit, or disruption, correlation and/or synchrony changes may have for autistic mouse models of cortical sensory processing, that are independent of rate alone, is an interesting topic on which our data only begins to touch.

The disruption of E-I balance has been implicated in schizophrenia, autism and intellectual disabilities. It has previously been suggested[39] that autism and other related disorders might reflect an increase in the ratio between excitation and inhibition that leads to hyperexcitability of cortical circuits. Similarly, E-I balance is thought to be disrupted in epilepsy. It is worth noting that autistic individuals develop epilepsy at a rate up to 25 times that of the general population[40]. We did not observe spontaneous epileptic seizures in *Shank3B*$^{-/-}$ mice. Nevertheless, excitatory neurons of primary sensory cortex (S1) were hyperexcitable and interneuron activity was reduced, suggesting a disruption of E-I balance. Furthermore, we found in *Shank3B*$^{-/-}$ mice showed differences in perceptual performance and evoked responses of the excitatory neurons only for weaker whisker deflections, not in strong deflections. However, there was a difference in the evoked response of inhibitory neurons in *Shank3B*$^{-/-}$ mice even for strong stimuli. We also found a difference in the perceptual performance and evoked responses of the excitatory neurons both in weaker and strong deflections where we knocked *Shank3B* from just vS1 interneurons of adult mice. Together, these results suggest that the nervous system of *Shank3B*$^{-/-}$ mice may have compensated during development in order to normalize the representations of strong sensory stimuli, despite having less inhibition to work with. There are many possible ways to achieve this; one parsimonious explanation is lemniscal-thalamic drive to S1 may have been downregulated in development to achieve similar sensory responses in the cortex for the most unambiguous stimuli. Understanding more of how the central nervous system contributes as a whole to ASD phenotypes is an interesting topic for further study.

Online content

Any methods, additional references, Nature Research reporting summaries, source data, extended data, supplementary information, acknowledgements, peer review information; details of author contributions and competing interests; and statements of data and code availability are available at https://doi.org/10.1038/s41593-020-0598-6.

Received: 6 August 2018; Accepted: 27 January 2020;
Published online: 02 March 2020

References

1. Amso, D., Haas, S., Tenenbaum, E., Markant, J. & Sheinkopf, S. J. Bottom-up attention orienting in young children with autism. *J. Aut. Dev. Disord.* **44**, 664–673 (2014).
2. Leekam, S. R., Nieto, C., Libby, S. J., Wing, L. & Gould, J. Describing the sensory abnormalities of children and adults with autism. *J. Aut. Dev. Disord.* **37**, 894–910 (2007).
3. Wang, A. T. et al. Neural selectivity for communicative auditory signals in Phelan-McDermid syndrome. *J. Neurodev. Disord.* **8**, 5 (2016).
4. Gogolla, N., Takesian, A. E., Feng, G., Fagiolini, M. & Hensch, T. K. Sensory integration in mouse insular cortex reflects GABA circuit maturation. *Neuron* **83**, 894–905 (2014).
5. Goncalves, J. T., Anstey, J. E., Golshani, P. & Portera-Cailliau, C. Circuit level defects in the developing neocortex of Fragile X mice. *Nat. Neurosci.* **16**, 903–909 (2013).
6. Chao, H. T. et al. Dysfunction in GABA signalling mediates autism-like stereotypies and Rett syndrome phenotypes. *Nature* **468**, 263–269 (2010).
7. Zhang, Y. et al. Dendritic channelopathies contribute to neocortical and sensory hyperexcitability in *Fmr1*(-/*y*) mice. *Nat. Neurosci.* **17**, 1701–1709 (2014).
8. Orefice, L. L. et al. Peripheral mechanosensory neuron dysfunction underlies tactile and behavioral deficits in mouse models of ASDs. *Cell* **166**, 299–313 (2016).
9. Peca, J. et al. Shank3 mutant mice display autistic-like behaviours and striatal dysfunction. *Nature* **472**, 437–442 (2011).
10. Naisbitt, S. et al. Shank, a novel family of postsynaptic density proteins that binds to the NMDA receptor/PSD-95/GKAP complex and cortactin. *Neuron* **23**, 569–582 (1999).
11. Bozdagi, O. et al. Haploinsufficiency of the autism-associated *Shank3* gene leads to deficits in synaptic function, social interaction, and social communication. *Mol. Aut.* **1**, 15 (2010).
12. Mei, Y. et al. Adult restoration of Shank3 expression rescues selective autistic-like phenotypes. *Nature* **530**, 481–484 (2016).
13. Wang, X. et al. Altered mGluR5-Homer scaffolds and corticostriatal connectivity in a Shank3 complete knockout model of autism. *Nat. Commun.* **7**, 11459 (2016).
14. Wang, X. et al. Synaptic dysfunction and abnormal behaviors in mice lacking major isoforms of Shank3. *Hum. Mol. Genet.* **20**, 3093–3108 (2011).
15. Siegle, J. H., Pritchett, D. L. & Moore, C. I. Gamma-range synchronization of fast-spiking interneurons can enhance detection of tactile stimuli. *Nat. Neurosci.* **17**, 1371–1379 (2014).
16. Luo, T. Z. & Maunsell, J. H. Neuronal modulations in visual cortex are associated with only one of multiple components of attention. *Neuron* **86**, 1182–1188 (2015).
17. Goel, A. et al. Impaired perceptual learning in a mouse model of Fragile X syndrome is mediated by parvalbumin neuron dysfunction and is reversible. *Nat. Neurosci.* **21**, 1404–1411 (2018).
18. de la Rocha, J., Doiron, B., Shea-Brown, E., Josic, K. & Reyes, A. Correlation between neural spike trains increases with firing rate. *Nature* **448**, 802–806 (2007).
19. Chen, T. W. et al. Ultrasensitive fluorescent proteins for imaging neuronal activity. *Nature* **499**, 295–300 (2013).
20. Doiron, B., Litwin-Kumar, A., Rosenbaum, R., Ocker, G. K. & Josic, K. The mechanics of state-dependent neural correlations. *Nat. Neurosci.* **19**, 383–393 (2016).
21. Peron, S. P., Freeman, J., Iyer, V., Guo, C. & Svoboda, K. A cellular resolution map of barrel cortex activity during tactile behavior. *Neuron* **86**, 783–799 (2015).
22. Crochet, S., Poulet, J. F., Kremer, Y. & Petersen, C. C. Synaptic mechanisms underlying sparse coding of active touch. *Neuron* **69**, 1160–1175 (2011).
23. Yang, H., Kwon, S. E., Severson, K. S. & O'Connor, D. H. Origins of choice-related activity in mouse somatosensory cortex. *Nat. Neurosci.* **19**, 127–134 (2016).
24. Kim, E. & Sheng, M. PDZ domain proteins of synapses. *Nat. Rev. Neurosci.* **5**, 771–781 (2004).
25. Kouser, M. et al. Loss of predominant Shank3 isoforms results in hippocampus-dependent impairments in behavior and synaptic transmission. *J. Neurosci.* **33**, 18448–18468 (2013).
26. Cruikshank, S. J. et al. Thalamic control of layer 1 circuits in prefrontal cortex. *J. Neurosci.* **32**, 17813–17823 (2012).
27. Moore, C. I. & Nelson, S. B. Spatio-temporal subthreshold receptive fields in the vibrissa representation of rat primary somatosensory cortex. *J. Neurophysiol.* **80**, 2882–2892 (1998).
28. Wehr, M. & Zador, A. M. Balanced inhibition underlies tuning and sharpens spike timing in auditory cortex. *Nature* **426**, 442–446 (2003).
29. Orefice, L. L. et al. Targeting peripheral somatosensory neurons to improve tactile-related phenotypes in ASD models. *Cell* **178**, 867–886 e824 (2019).
30. Dimidschstein, J. et al. A viral strategy for targeting and manipulating interneurons across vertebrate species. *Nat. Neurosci.* **19**, 1743–1749 (2016).
31. Sachidhanandam, S., Sermet, B. S. & Petersen, C. C. H. Parvalbumin-expressing GABAergic neurons in mouse barrel cortex contribute to gating a goal-directed sensorimotor transformation. *Cell Rep.* **15**, 700–706 (2016).
32. Goffin, D., Brodkin, E. S., Blendy, J. A., Siegel, S. J. & Zhou, Z. Cellular origins of auditory event-related potential deficits in Rett syndrome. *Nat. Neurosci.* **17**, 804–806 (2014).
33. Selby, L., Zhang, C. & Sun, Q. Q. Major defects in neocortical GABAergic inhibitory circuits in mice lacking the fragile X mental retardation protein. *Neurosci. Lett.* **412**, 227–232 (2007).
34. O'Neill, M. & Jones, R. S. Sensory-perceptual abnormalities in autism: a case for more research? *J. Aut. Dev. Disord.* **27**, 283–293 (1997).
35. Marco, E. J., Hinkley, L. B., Hill, S. S. & Nagarajan, S. S. Sensory processing in autism: a review of neurophysiologic findings. *Pediatr. Res.* **69**, 48R–54R (2011).
36. Lee, J. et al. *Shank3*-mutant mice lacking exon 9 show altered excitation/inhibition balance, enhanced rearing, and spatial memory deficit. *Front. Cell. Neurosci.* **9**, 94 (2015).
37. Tu, J. C. et al. Coupling of mGluR/Homer and PSD-95 complexes by the Shank family of postsynaptic density proteins. *Neuron* **23**, 583–592 (1999).

38. Peixoto, R. T., Wang, W., Croney, D. M., Kozorovitskiy, Y. & Sabatini, B. L. Early hyperactivity and precocious maturation of corticostriatal circuits in *Shank3B*$^{-/-}$ mice. *Nat. Neurosci.* **19**, 716–724 (2016).
39. Rubenstein, J. L. & Merzenich, M. M. Model of autism: increased ratio of excitation/inhibition in key neural systems. *Genes Brain Behav.* **2**, 255–267 (2003).
40. Bolton, P. F. et al. Epilepsy in autism: features and correlates. *J. Ment. Sci.* **198**, 289–294 (2011).

Methods

Animal use. All experiments were conducted under the guidelines of the Division of Comparative Medicine, with the protocol approved by the Committee for Animal Care of the Massachusetts Institute of Technology. *Shank3B*$^{-/-}$ and *Shank3B* conditional knockout mouse line was generated by our lab as described in previous study[9,29] and bred in house on a 12 h light/dark cycle (lights on at 07:00, lights off at 19:00) with food and water available ad libitum. A mix of male and female C57BL/6 mice (4–6 months old) were used for experiments. All experiments using *Shank3B*$^{-/-}$ mice were performed in age-matched littermates from breeding pairs between *Shank3B*$^{+/-}$ heterozygous animals. All animal experiments and data analysis were performed with experimenters blinded to genotypes.

Uncued tactile behavioural test. *Surgeries.* On the day of surgery, mice were induced into an anesthetic state with 3% isoflurane (in O_2) and injected with 0.1 mg kg^{-1} intraperitoneal buprenorphine (an opiate analgesic). Meloxicam (1 mg kg^{-1}, subcutaneous) was administered pre-operatively and every 24 h for 3 days to reduce inflammation. Isoflurane was lowered until mice reached a stable anaesthetic plane, at which time the isoflurane was typically 1.5–2%. The head was shaved from the nasal septum up to the occipital bone (between ears) and ointment applied to each eye. The mouse was positioned in a stereotactic head holder/gas mask. The surgical area was cleaned by 70% alcohol and 2% iodine solution. The scalp overlying the dorsal skull was removed. The periosteum was removed with a scalpel. An autoclaved titanium headpost was cemented to the exposed skull using strong dental cement (C&B Metabond; Parkell). After head plate implantation, mice recovered for at least five days before beginning water restriction. ~4–6-month-old male and female WT ($n=15$) and *Shank3B*$^{-/-}$ ($n=17$) mice were used for the behavior test. For locally deleting *Shank3B* from the interneurons in vS1, ~4-month-old male and female *Shank3B*$^{fl/fl}$ mice ($n=11$) were unilaterally injected with $AAV_{2/8}$-Dlx5/6-Cre-mKate2 or $AAV_{2/8}$-Dlx5/6-ΔCre-mKate2 (control, $n=11$) in vS1 and the head plate was implanted. For locally deleting *Shank3B* from the excitatory neurons in vS1, ~4-month-old male and female *Shank3B*$^{fl/fl}$ mice were unilaterally injected with $AAV_{2/8}$-CaMKII-Cre-mKate2 ($n=9$) or $AAV_{2/8}$-CaMKII-ΔCre-mKate2 (control, $n=7$). For chemogenetic inhibition of inhibitory neurons in vS1, 3–4-month-old male and female WT mice were unilaterally injected with $AAV_{2/9}$-Dlx5/6-hM4Di-p2a-nlsdTomato ($n=8$) or $AAV_{2/9}$-Dlx5/6-dTomato-p2a-nlsdTomato (control, $n=8$). Mice recovered for two weeks to allow virus expression before the beginning of water restriction.

Behavior/water restriction. Animals were placed on water restriction for at least seven days (1–1.25 ml per day) before training. We interacted with animals almost daily as they were habituated to the behavioral apparatus and the researcher. Whiskers were restrained by placing them in a hoop made from silk suture thread that was closed 2–3 mm from the base of the whiskers. This restrainer was attached to a piezo-electric plate bender (Noliac; CMBP09). At the beginning and end of each session, we confirmed that the restrainer was in the same place and held the same whiskers as when the experiment started. On the first two days of training, we focused on associating licking from an acrylic lick-port with whisker stimulation. After this conditioning session (100–200 trials), mice performed our behavioral task with 300–400 trials of mostly highly perceptible stimuli. Once they displayed proficiency with the task (signal detection statistic for strong stimuli, $d' > 1$), all sessions were converted to 20% catch trials and stimuli drawn from a random interval allowing for coverage over their entire perceptible range. Mice typically ran 12–14 sessions before being taken off water restriction. The data collection was randomized. Mice were rotated across behavioral rigs between each session to avoid any biasing of behavior toward a specific rig. Further, the training sequence of the animals was randomized across training days. For the chemogenetic manipulations, mice were trained for 11 sessions before the administration of the C21[41] (2 mg kg^{-1}, intraperitoneal injection, HelloBio). From sessions 12 to 14, mice were administrated with C21 1 h before the training.

Behavioral control was conducted using custom routines written in MATLAB (Mathworks) to interface with National Instruments DAQ boards. The piezo actuator was controlled by piezo driver (Noliac). The stimulus was a 20 Hz train of ten stimuli that each consisted of a fast cosine wave onset with a time to peak of 6 ms (from caudal to rostral) and a slow cosine return with a time to peak of 20 ms (from the deflected rostral point back to rest). For maximum-amplitude deflections, vibrissae moved approximately 1 mm at the point of contact. The stimulation amplitudes were calibrated using a high-speed camera. Lick detection was made using an IR emitter/receiver pair (SparkFun; SEN-00241) centered across the tip of the lick-spout; the IR pair was calibrated daily. Solenoid valves (NResearch; 161T011) gated water flow and vacuum return.

There were no stimulus cues and all behaviors were done in a dark room with white masking noise present. Stimulus timing was essentially random: each trial had a fixed time of 8 s from a behavioral control perspective, but we randomly chose a time to insert a stimulus between 1 and 6 s after trial onset. The stimulus amplitude was chosen randomly except for catch trials (stimulus amplitude = 0 mm) and maximal stimuli (stimulus amplitude=1 mm were interleaved randomly, but had a fixed frequency. In addition, any false alarms (licking during the report window on a catch trial) led to 20 s time out.

Data analysis: No mice or data points from our experimental groups were excluded from analysis. Trials were included for analysis from behavioral sessions in which mice just began to show proficiency in the task, were engaged with the task, and completed at least fifty trials without pre-stimulus licking. We excluded trials where animals licked 500 ms before the onset of a stimulus. Trials for detection tasks are not initiated by the subject. Thus, the number of trials that mice would complete in a session was dependent on their experience and motivation. We had a maximum amount of time would allow any mouse to stay on a rig, but all mice would complete their trials before this time elapsed. However, because the number of trials each mouse would complete was variable, we allowed mice to run until they abstained from licking over a large block of trials, regardless of how detectable the stimulus was, which we interpreted as the animal disengaging from the task. In some cases, a mouse would disengage for a noticeable block of trials, but then re-engage. We developed an empirical method to detect the period(s) in which the mouse disengaged from the task and used it to set an 'engagement threshold' to exclude disengaged trials. This method involved taking the moving average of the binary responses and stimulus amplitude using a 50-trial wide window. This resulted in a time series showing 50-trial wide trends in response probability and stimulus amplitude fluctuations. As mice reached the end of a session, their average response rate would begin to slowly drift towards zero and skew the response distribution towards zero. We empirically determined that the amount of skew (difference in median and mean) of the stimulus distribution, relative to its bottom third was similar to the proportion of skew in the response distribution and its bottom third when disengaged trials at the end of a session were manually removed. Thus, we defined an engagement threshold as the bottom third of the response distribution corrected for the proportional difference between its statistics and that of the stimulus distribution. Any block of trials that were below this line were excluded from analysis.

Psychometric curve construction: Psychometric curves show the relationship between stimulus amplitude and detection rate. To test if these curves were different between *Shank3B*$^{-/-}$ mice we compared the mid-points (threshold) and slope factors (k) of the curve fits for each mouse. The 'threshold' in this case corresponds to the deflection amplitude that leads to a successful report more than half of the time, relative to the false alarm rate. We binned responses (hits or misses) based into one of five stimulus amplitude bins. We similarly grouped false alarms and correct rejections for all catch trials (trials with a zero-amplitude stimulus). We computed the hit rate for each amplitude bin, and the false-alarm rate and fit a sigmoidal function to the resulting amplitude versus response rate data. The sigmoidal function of the form: $y = \max/(\max + e^{(\text{threshold}-X)/\text{slopeFactor})})$, where X is the independent variable (stimulus amplitude) and the fit parameters are: (1) the threshold, which is the amplitude that leads to 50% of the maximal response, (2) max, which is the maximal response, and (3) slope factor, which is the slope of the resulting sigmoid near the threshold. Curve fits were performed in MATLAB using a non-linear least squares method. All fits had an adjusted $R^2 > 0.95$ and a threshold within our stimulus range.

Virus injection and cranial window preparation. Mice were anesthetized using isoflurane (3% for induction, 1.5–2% during surgery). and injected with 0.1 mg kg^{-1} IP buprenorphine (an opiate analgesic). Meloxicam (1 mg/kg, subcutaneous) was administered pre-operatively and every 24 h for 3 days to reduce inflammation. The head is shaved from the nasal septum up to the occipital bone (between ears) and ointment is applied to each eye. The mouse is positioned in a stereotactic head holder/gas mask. The surgical area is cleaned by 2% iodine and 70% alcohol solution. The scalp overlying the dorsal skull was removed. The periosteum was removed with a scalpel. A 3 × 3 mm piece of skull was removed above the somatosensory cortex as determined by stereotactic coordinates, and the dura was kept intact and moist with saline.

To express GCaMP6f in pyramidal neurons of the primary somatosensory cortex, adeno-associated virus AAV2/8 carrying the construct CaMKII-GCaMP6f (GCaMP6f under the neural-specific human CaMKIIα promoter, 1×10^{12} genome copies per ml) was injected at a depth of ~200 µm to the primary somatosensory cortex (5~6 sites, the center of the injection area is: 1.5 mm post the lambda suture, 2.5 mm from the mild line suture) of adult male and female C57BL/6 J WT and *Shank3B*$^{-/-}$ mice (4–6-month-old, $n=6$ in each groups). For expression of GCaMP6 in GABAergic neurons, GCaMP6 in AAV2/8 under the Dlx5/6 promoter was injected in the primary somatosensory cortex of 4–6-month-old male and female WT and *Shank3B*$^{-/-}$ mice ($n=6$ in each groups). For conditional knockout *Shank3* in interneurons and imaging neuronal activity in inhibitory or excitatory neurons in *Shank3B*$^{fl/fl}$ mice, $AAV_{2/8}$-Dlx5/6-GCaMP6 or $AAV_{2/8}$-CaMKII-GCaMP6 virus and AAV-Dlx5/6-Cre-mKate2 were injected into the somatosensory cortex at a ratio of 1:3. Small volumes (~20 nl) of viral suspension were delivered over a period of 5 min per site using a Nanoject II micro-injector (Drummond scientific, Broomall, PA, USA).

For the cranial window, two coverslips were joined with ultraviolet curable optical glue (NOR-138, Norland). A smaller (3 mm diameter) insert fit into the craniotomy and a larger piece (5 mm diameter) was attached to the bone. A custom-designed head plate was cemented on the cranial window with Metabond (Parkell).

In vivo two-photon calcium imaging. To reduce the anxiety behavior related to the head fixed strategy, we let the animal adapt the imaging environment prior to

imaging. Two weeks after viral injection mice were moved to two-photon imaging room and each mouse was head fixed on a custom-made mouse strain system for 30 min, once per day for five days. For each imaging experiment, mice were head fixed in the restraint and placed under the two-photon microscope for 15 min before the experiments started. Mice were imaged two rounds of spontaneous firing without whisker stimulation. And the mice were imaged with the whisker stimulation driven by piezo after the mice trained (4–5 weeks after virus injection). The stimulation method and rigs were identical to the tactile detection behavior test.

In vivo two-photon imaging was performed as described previously[42]. Briefly, the imaging was performed on a custom two-photon laser-scanning microscope (Ultima; Bruker) coupled with a Mai Tai Deep See laser (Spectra Physics). The laser was operated at 910 nm (~30–40 mW average power on the sample). The emission filter set for imaging GCaMP6 fluorescence consisted of a 575-nm dichroic mirror and a 525/70 nm band-pass filter. Fluorescence signal was detected using Hamamatsu multialkali PMTs. In most experiments, images were acquired at frame rates of 10 Hz at a resolution of 128 × 100 pixels using a ×20, 1.0 NA water-immersion objective (Zeiss). Image acquisition was performed using custom Prairie View Software. We collected 15 min of spontaneous activity to estimate the occurrence and duration of spontaneous events. Then, the same stimuli used in the un-cued tactile behavioral test were delivered to the contralateral whiskers and GCaMP6 signals were simultaneously recorded.

Calcium imaging data analysis. Images were analyzed *post hoc* using a custom program, and open-source routines, written using MATLAB (MathWorks). The package has been used elsewhere[43] and is available via GitHub (https://github.com/cdeister/imageAnalysis_gui). Frames were collected as individual image files. For analyses of spontaneous calcium events, we collected 8,752 images per mouse at 10 Hz. We analyzed the first 10 min of each recording to compute event rate, which comprise 6,000 images per mouse. For analyses of stimulus-evoked response, 70 images were acquired for 300 trials for a total of 21,000 frames per mouse. Most motion artifacts came from small movements in the x-y plane. Because our acquisition rate was faster than the average frequency of mouse movements, we relied on rigid-body methods to align images[44]. We used a discrete Fourier transform based method that calculated shifts with sub-pixel increments. A registration template was constructed from averaging the first 10–100 images collected, or 10–100 images that had the lowest luminance value; both methods resulted in similarly stable images. Each image was aligned to the template. Mean and standard deviation projections of the registered stack were made, from which somatic regions of interests (ROIs) were made using semi-automated segmentation of factors found using non-negative matrix factorization. All ROIs were inspected manually. A binary mask from the segmented regions was made for later processing. Fluorescence values were extracted from each ROI for each frame, and the mean for each cell was computed. In addition, we made annulus-shaped ROIs to estimate neuropil contamination by eroding out 15 pixels from each somatic ROI and subtracting any other cell body that fell in this ring. This gave us two vectors of fluorescence values for the soma and the neuropil. We weighted the neuropil vector by 0.8, which was on the high side of contamination estimates we made by comparing the difference in blood vessels and their surround[45]. The weighted neuropil vector was subtracted from the somatic vector to produce a corrected vector of fluorescence values.

Fluorescence value (F) traces were converted to a normalized $\Delta F/F$ trace. We used an approach similar to previous population calcium imaging studies to estimate baseline F_0 fluorescence in each cell. F_0 computed via a sliding-window of 500 frames (approximately 50 s) using a quartile cut-off that ranged from the bottom tenth percentile up to the median, depending on how active the neuron was[46]. Lastly, F and F_0 traces were used to make the final $\Delta F/F$ trace given by $(F(i)-F_0(i))/F_0(i))$, where i is the index for each frame. Records of $\Delta F/F$ were grouped into trials and aligned to stimulus onsets for behavioral data for further analysis. We excluded neurons with filled nuclei, which we determined during segmentation by looking at time-lapse movies as well as average and variance projection images. We also looked for disproportionately long decay-time for spontaneous transients as an indication of filled neurons. These neurons comprised at most 1.5% of our imaging fields.

We defined stimulus responsive neurons as those whose evoked-GCaMP6 $\Delta F/F$ values (the magnitude of $\Delta F/F$ integrated over 500 ms post-stimulus minus the baseline $\Delta F/F$ integrated over 500 ms pre-stimulus), averaged across trials with 0.75–1.00 mm deflection amplitudes (the higher end of the detectable range), differed significantly ($P < 0.05$; bootstrap mean-difference test) than evoked activity averaged across trials with a zero-amplitude stimulus.

We estimated event rate by counting the total number of deconvolved events from the resulting $\Delta F/F$ traces using a robust non-negative deconvolution method[47,48] implemented in MATLAB (https://github.com/zhoupc/OASIS_matlab). Event rate was defined as the number of individual Ca^{2+}-transients discharged in a 10-min period. The algorithm has few hand-tunable parameters, but it takes a 'Noise Factor' for thresholding noise and signal during its pre-processing steps. We empirically determined this factor for excitatory and inhibitory cells separately and found that a factor of 1 for excitatory cells and 5 for inhibitory cells to result in 'de-noised' ΔF/F traces that were closest to visually inspect raw data. We swept the range of noise factors for all neurons analyzed and computed the R^2 value between raw data and the algorithm's processed data and observed that R^2 peaked at 0.99 at our chosen noise factor values, but were largely stable over a wide range of values.

Correlation coefficients were computed as the Spearman's rank correlation coefficient (ρ) using the built-in MATLAB 'corr' function. To construct distributions of correlations in spontaneous activity, we computed ρ for all possible pairings of neurons deemed active at all (showed at least ten calcium events in 10 min, for example rate >0.01 Hz), for all of an experimental group's spontaneous firing imaging sessions, which were then pooled. P values for ρ were determined using the same Matlab function, which computes the tail-probability of the Spearman 'D-statistic'.

PSTHs were made by determining the average evoked response across six different amplitudes of whisker deflections, including the zero-amplitude stimuli. We did this for all stimulus responsive neurons and converted ΔF/F to standard scores (Z-scores), which allowed us to determine the degree to which the magnitude of evoked responses differed between groups despite differences in their baseline spontaneous activity.

In vitro electrophysiology and single-cell genotyping. *Slice preparation.* The slice preparations were followed by previously described. Briefly, the mice injected with $AAV_{2/8}$-CaMKII-GCaMP6 and $AAV_{2/8}$-Dlx5/6-Cre-mKate2 were anesthetized via isoflurane and transcardially perfused with 20 ml of ice-cold carbogenated (95% O_2 and 5% CO_2,) cutting solution containing 194 mM sucrose, 30 mM NaCl, 4.5 mM KCl, 1.2 mM NaH_2PO_4, 0.2 mM $CaCl_2$, 2 mM $MgCl_2$, 26 mM $NaHCO_3$, and 10 mM D-(+)-glucose (with osmolarity of 300–305 mOsm l^{-1}). The brain was rapidly removed and placed into ice-cold cutting solution for slice preparation. The coronal slices (300 µm) containing the somatosensory cortex were prepared by a slicer (VT1200S, Leica, Germany) and then incubated in a holding chamber at 32 °C for 15–20 min. Then the slices were transferred to artificial cerebral spinal fluid containing 136 mM NaCl, 3.5 mM KCl, 1 mM $MgCl_2$, 2.5 mM $CaCl_2$, 26 mM $NaHCO_3$ and 11 mM glucose (with osmolarity of 295–300 mOsm l^{-1}) at room temperature for at least 1 h.

Electrophysiological recordings. Whole-cell patch clamp recordings were performed with infrared differential interference contrast visualization at room temperature (21–25 °C). The fluorescently labeled neurons were visualized and identified with a microscope equipped with GCaMP6 or red fluorescent protein (mKate2) filter (BX-51WI, Olympus). Recording pipettes (BF150-86-7.5, Sutter Instruments) were pulled in a horizontal pipette puller (P-97, Sutter Instruments) with a tip resistance of 3–5 MΩ. Patch pipettes were filled with a solution containing 128 mM potassium gluconate, 10 mM Hepes, 10 mM phosphocreatine sodium salt, 1.1 mM EGTA, 5 mM ATP magnesium salt, and 0.4 mM GTP sodium salt. pH was adjusted to 7.3 with KOH, and osmolarity was adjusted to 300–305 mOsm with sucrose. An axon 700B amplifier (Molecular Devices) was used to record membrane potentials. Signals were low-pass filtered at 5 kHz and sampled at 20 kHz with a Digidata 1550 and Clampex 10.6 (Molecular Devices), and data were stored on a computer for subsequent offline analysis.

Single-cell collection and PCR. To collect intact single cell and minimal the contamination, we cleaned all work surfaces and equipment with DNA-OFF (Takara Cat. #9036). Pipettes of 2–4 MΩ resistance were filled with intracellular solution (the same recipe with electrorheological recordings). We gave a positive pressure before attaching the cell. When the pipette touching the neuron, we removed the positive pressure immediately and applied light suction until the cell had visibly clung to the tip of pipette. Then pick up the cell slowly and gently under the guidance of microscope, seeing the detachment of the cell from the slice. After that, we broke the tip of the pipette in the PCR tube containing 4 µl of 1× PBS buffer and snap frozen on dry ice. The samples were transferred to −80 °C until further processing. According to the recommended protocols single-cell gDNA samples were amplified by REPLI-g Single Cell Kit (Qiagen). Briefly, the single cell solution was taken out from −80 °C and added 3 µl of Buffer D2. Samples were incubated for 10 min at 65 °C and the reaction was stopped by adding of 3 µl of Stop buffer. Samples were incubated for another 10 hs at 30 °C after adding the amplification mix (29 µl buffer, 2 µl REPLI sc DNA polymerase) and at 65 °C for 10 min. After amplification, the products were used for PCR analysis. The PCR primers are: F1: 5′-CAGCATTTATACCTGACTGTGAAGC-3′, R1: 5′ -GGGAGTAGAGCTCAGATAACC-3′ and R2: 5′-CTTTGTAAGACCAAAGTGTGG-3′. The PCR amplification conditions are: 95 °C for 5 min, 95 °C, 30 s; 58 °C, 30 s; 58 °C, 60 s; for 35 cycles, 72 °C for 5 min. The PCR products were running on 2% agarose gels.

Statistics. All comparisons between groups were collected from littermate animals with experiments performed at the same time. No statistical methods were used to predetermine sample sizes, but our sample sizes are similar to those reported in previous publications[9,12]. With few exceptions, hypothesis testing between two groups using a bootstrap mean-difference test that does not assume the underlying data are normally distributed. For these tests, we computed a bootstrap distribution of the difference in the two group's means, for each of 10,000 permutations. Normality of the resulting bootstrap distribution was determined

by comparing it to a randomly sampled normal distribution with the same mean and standard deviation as the bootstrap distribution. We used the confidence intervals of the resulting bootstrap distribution to derive *P* values[49]. We report all *P* values greater than 0.0001 as the actual *P* value, but those less than 0.0001 are reported as $P < 0.0001$. Throughout the study, we used $P < 0.05$ as threshold for rejecting the null-hypothesis. Calculation of the statistics was done in MATLAB 2018b (Mathworks). Further details on particular statistical analyses can be found on the respective figures/results section for each dataset. In two experiments we performed a two-tailed, unpaired Student's *t*-test using Prism 7 (GraphPad Software); for those experiments we did not formally test for normality and equal variance, but assumed the data were normally distributed and had equal variance. In those two cases, we show the underlying data points or distribution. Experiments were randomized and the investigators were blind to the genotypes during the experiments and outcome assessment.

Reporting Summary. Further information on research design is available in the Nature Research Reporting Summary linked to this article.

Data Availability

Raw data is available from the corresponding author upon request.

Code Availability

The custom routines for image analysis written in MATLAB are available on GitHub (https://github.com/cdeister/imageAnalysis_gui) and from the corresponding author upon request.

References

41. Thompson, K. J. et al. DREADD agonist 21 is an effective agonist for muscarinic-based DREADDs in vitro and in vivo. *ACS Pharmacol. Transl. Sci.* **1**, 61–72 (2018).
42. Chen, Q. et al. Imaging neural activity using *Thy1-GCaMP* transgenic mice. *Neuron* **76**, 297–308 (2012).
43. Truszkowski, T. L. A cellular mechanism for inverse effectiveness in multisensory integration. *eLife* **6**, e25392 (2017).
44. Guizar-Sicairos, M., Thurman, S. T. & Fienup, J. R. Efficient subpixel image registration algorithms. *Opt. Lett.* **33**, 156–158 (2008).
45. Kerlin, A. M., Andermann, M. L., Berezovskii, V. K. & Reid, R. C. Broadly tuned response properties of diverse inhibitory neuron subtypes in mouse visual cortex. *Neuron* **67**, 858–871 (2010).
46. Komiyama, T. et al. Learning-related fine-scale specificity imaged in motor cortex circuits of behaving mice. *Nature* **464**, 1182–1186 (2010).
47. Pachitariu, M., Stringer, C. & Harris, K. D. Robustness of spike deconvolution for neuronal calcium imaging. *J. Neurosci.* **38**, 7976–7985 (2018).
48. Friedrich, J., Zhou, P. & Paninski, L. Fast online deconvolution of calcium imaging data. *PLoS Comput. Biol.* **13**, e1005423 (2017).
49. Altman, D. G. & Bland, J. M. How to obtain the confidence interval from a *P* value. *Brit. Med. J.* **343**, d2090 (2011).

Acknowledgements

We thank J. Wilde, A. Krol, M. G. Chen, M. Hu and members of the Feng Lab for helpful discussions. We thank D. A. Scott, S. Allsop, B. Clear and T. Dalia for technical support. We thank the Varanasi Family and R. Buxton for supporting our autism research. This work was supported by the Hock E. Tan and K. Lisa Yang Center for Autism Research at MIT, the Stanley Center for Psychiatric Research at the Broad Institute of MIT and Harvard, Nancy Lurie Marks Family Foundation, the Poitras Center for Psychiatric Disorders Research at the McGovern Institute for Brain Research at MIT, Shenzhen Overseas Innovation Team Project No. KQTD20140630180249366 (Z.L.); Guangdong Innovative and Entrepreneurial Research Team Program No. 2014ZT05S020 (Z.L.) and the National Institutes of Health R01MH097104 (G. Feng), NIMH Conte Center grant P50MH094271 (G. Feng), F32MH100749 (C.A.D.) and R01NS045130 (C.I.M.).

Author contributions

Q.C., C.A.D., C.I.M. and G. Feng designed experiments and wrote the paper. Q.C., C.A.D., X.G., B.G., T.L.J., N.C. and R.L. performed experiments. C.A.D. wrote the MATLAB code and did the data analysis. M.F.W. generated *Shank3B* conditional knockout mouse. S.F., Z.L., M.J.G., Y.S. and W.L. did part of data analysis and interpretation. J.D. and G. Fishell designed and provided the Dlx5/6 promoter.

Competing interests

The authors declare no competing interests.

Additional information

Supplementary information is available for this paper at https://doi.org/10.1038/s41593-020-0598-6.

Correspondence and requests for materials should be addressed to C.I.M. or G.F.

Peer review information *Nature Neuroscience* thanks D. Feldman and the other, anonymous, reviewer(s) for their contribution to the peer review of this work.

Reprints and permissions information is available at www.nature.com/reprints.

nature research

Corresponding author(s): Christopher I. Moore, Guoping Feng

Reporting Summary

Nature Research wishes to improve the reproducibility of the work that we publish. This form provides structure for consistency and transparency in reporting. For further information on Nature Research policies, see Authors & Referees and the Editorial Policy Checklist.

Statistical parameters

When statistical analyses are reported, confirm that the following items are present in the relevant location (e.g. figure legend, table legend, main text, or Methods section).

n/a	Confirmed	
☐	☒	The exact sample size (*n*) for each experimental group/condition, given as a discrete number and unit of measurement
☐	☒	An indication of whether measurements were taken from distinct samples or whether the same sample was measured repeatedly
☐	☒	The statistical test(s) used AND whether they are one- or two-sided *Only common tests should be described solely by name; describe more complex techniques in the Methods section.*
☐	☒	A description of all covariates tested
☐	☒	A description of any assumptions or corrections, such as tests of normality and adjustment for multiple comparisons
☐	☒	A full description of the statistics including central tendency (e.g. means) or other basic estimates (e.g. regression coefficient) AND variation (e.g. standard deviation) or associated estimates of uncertainty (e.g. confidence intervals)
☐	☒	For null hypothesis testing, the test statistic (e.g. *F*, *t*, *r*) with confidence intervals, effect sizes, degrees of freedom and *P* value noted *Give P values as exact values whenever suitable.*
☒	☐	For Bayesian analysis, information on the choice of priors and Markov chain Monte Carlo settings
☒	☐	For hierarchical and complex designs, identification of the appropriate level for tests and full reporting of outcomes
☐	☒	Estimates of effect sizes (e.g. Cohen's *d*, Pearson's *r*), indicating how they were calculated
☐	☒	Clearly defined error bars *State explicitly what error bars represent (e.g. SD, SE, CI)*

Our web collection on statistics for biologists may be useful.

Software and code

Policy information about availability of computer code

Data collection	Behavioral control was conducted using custom routines written in Matlab 2014b (Mathworks) to interface with National Instruments DAQ boards. The imaging was collected by a Prairie custom two-photon laser-scanning microscope software (Ultima; Prairie Technologies). Clampex 10.6 was used for eletrophysiological data acquisition.
Data analysis	Behavioral data was analyzed by custom written in Matlab 2018b (Mathworks). The two-photon imaging data was analyzed bycustom written in Matlab 2018b (Mathworks). The number of mKate2 and DAPI positive neurons in supplementary Figure 5 and 7 were analyzed using ImageJ (V1.48f, NIH). Clampfit 10.6 was used for eletrophysiological data off-line analysis. All statistical analyses were performed and plotted in Matlab 2018b and Prism7 (GraphPad Software) .

For manuscripts utilizing custom algorithms or software that are central to the research but not yet described in published literature, software must be made available to editors/reviewers upon request. We strongly encourage code deposition in a community repository (e.g. GitHub). See the Nature Research guidelines for submitting code & software for further information.

Data

Policy information about availability of data

All manuscripts must include a data availability statement. This statement should provide the following information, where applicable:

- Accession codes, unique identifiers, or web links for publicly available datasets
- A list of figures that have associated raw data
- A description of any restrictions on data availability

The custom routines for image analysis written in Matlab, are available on GitHub (https://github.com/cdeister/imageAnalysis_gui). Also, from the corresponding author upon request. Raw data could be obtained from corresponding author upon reasonable request.

Field-specific reporting

Please select the best fit for your research. If you are not sure, read the appropriate sections before making your selection.

☒ Life sciences ☐ Behavioural & social sciences ☐ Ecological, evolutionary & environmental sciences

For a reference copy of the document with all sections, see nature.com/authors/policies/ReportingSummary-flat.pdf

Life sciences study design

All studies must disclose on these points even when the disclosure is negative.

Sample size	Sample size for each experiment is indicated in the figure legend for each experiment. The sample size was chosen based on previous experience for each experiment to yield high power to detect specific effects. No statistical methods were used to predetermine sample size.
Data exclusions	No mice from our experimental groups were excluded from analysis.
Replication	The experiments reported in this work were repeated independently two to three times using different batches of animals.
Randomization	Animals were chosen based on correct genotyping. Each experiment contained animals from at least two different litters to ensure that the differences between genotypes can be observed in mice from different litters.
Blinding	During the execution and analyses of the behavioral experiments and in vivo two-photon imaging recordings,the investigators were blind to the genotypes of the individual animals.

Reporting for specific materials, systems and methods

Materials & experimental systems

n/a	Involved in the study
☒	☐ Unique biological materials
☒	☐ Antibodies
☒	☐ Eukaryotic cell lines
☒	☐ Palaeontology
☐	☒ Animals and other organisms
☒	☐ Human research participants

Methods

n/a	Involved in the study
☒	☐ ChIP-seq
☒	☐ Flow cytometry
☒	☐ MRI-based neuroimaging

Animals and other organisms

Policy information about studies involving animals; ARRIVE guidelines recommended for reporting animal research

Laboratory animals	A mix of male and female C57BL/6 mice (4~6-month-old) were used for experiments. Shank3B-/- and Shank3Bfl/fl mouse strains were produced in our lab at MIT. All experiments were conducted according to protocols approved by the Institutional Animal Care and Use and Institutional Biosafety Committees of MIT.
Wild animals	The study did not involved the wild animals.
Field-collected samples	The study did not involved the animal collected from field.